Propagation of insulator-to-metal transition driven by photoinduced strain waves in a Mott material

Tatsuya Amano, Danylo Babich, Ritwika Mandal, Julio Guzman-Brambila, Alix Volte, Elzbieta Trzop, Marina Servol, Ernest Pastor, Maryam Alashoor, Jörgen Larsson, et al.

Propagating insulator-to-metal transition in the wake of photoinduced strain waves in a Mott material

Tatsuya Amano[1], Danylo Babich[2], Ritwika Mandal[3], Julio Guzman-Brambila[2,3,8], Alix Volte[3,6,8], Elzbieta Trzop[3,9], Marina Servol[3,9], Ernest Pastor[3,9], Maryam Alashoor[3], Jörgen Larsson[6,7], Andrius Jurgilaitis[6], Van-Thai Pham[6], David Kroon[6], John Carl Ekström[6], Byungnam Ahn[6], Céline Mariette[8], Matteo Levantino[8], Mikhail Kozhaev[8], Julien Tranchant[2,9], Benoit Corraze[2,9], Laurent Cario[2,9], Mohammad Dolatabadi[2], Vinh Ta Phuoc[4,9], Rodolphe Sopracase[4], Mathieu Guillon[4], Hirotake Itoh[1,9], Yohei Kawakami[1,9], Yuto Nakamura[5], Hideo Kishida[5], Hervé Cailleau[3,9,*], Maciej Lorenc[3,9*], Shinichiro Iwai[1,9*], Etienne Janod[2,9*]

[1] Department of Physics, Tohoku University, Sendai 980-8578, Japan
[2] Nantes Université, CNRS, Institut des Matériaux de Nantes Jean Rouxel, IMN, F-44000 Nantes, France
[3] Univ Rennes, CNRS, IPR (Institut de Physique de Rennes) – UMR 6251, 35000 Rennes, France
[4] GREMAN—UMR 7347 CNRS, Université de Tours, Tours, France
[5]Department of Applied Physics, Graduate School of Engineering, Nagoya University, Nagoya, Aichi 464-8603, Japan
[6] MAX IV Laboratory, Lund University, P.O. Box 118, SE-221 00 Lund, Sweden
[7] Department of Physics, Lund University, P.O. Box 118, SE-221 00 Lund, Sweden
[8] ESRF, The European Synchrotron, 71 Avenue des Martyrs, CS40220, 38043 Grenoble Cedex 9, France
[9] CNRS, Univ Rennes, DYNACOM (Dynamical Control of Materials Laboratory) - IRL2015, The University of Tokyo, 7-3-1 Hongo, Tokyo 113-0033, Japan

* corresponding authors

Ultrafast physics opens new avenues for directing materials to different functional macroscopic states on non-thermal dynamical pathways. In any phase transition involving volume and/or ferroelastic deformation, an often overlooked mechanism emerges whereby photoinduced elastic waves drive the transition. However, a comprehensive physical picture of transformation dynamics which includes acoustic scale propagation remained elusive. Here we show that such strain wave mechanism drives the ultrafast insulator-to-metal phase transition (IMT) in granular thin films of the prototype Mott material V_2O_3. Based on time-resolved optical reflectivity and X-ray diffraction we evidence the role of strain wave mechanisms in ultrafast changes either with or without symmetry breaking. We reveal inverse ferroelastic shear occurring before the IMT propagating in the wake of compressive strain wave. These dynamics are shown to be governed by the domain size and the film thickness, respectively. A fluence threshold is evidenced for the onset of IMT at macroscopic scale, as well as phase separation at intermediate fluence and complete transformation at saturating fluence. We clarify the morphological conditions for the ultrafast IMT that is favoured in granular thin films, and hindered in single crystals. The

resulting physical picture sheds new light on the ultrafast phase transitions in quantum materials and future devices based on Mott insulators.

The ability to direct a material to another phase along a coherent transformation pathway raises questions on the dynamical limits of photoinduced phase transitions. This is particularly true in quantum materials where many transitions result from electron-lattice coupling. Thus, besides the well-known *optical* phonon coherent dynamics of charge density wave / Peierls systems [1-3], many electronic phase transitions exhibit volume change and/or shear deformations of the lattice. In such a situation, coherent dynamics operate through the propagation of strain waves, involving long-wavelength *acoustic* phonons.

In contrast with many coherent dynamics on the established transition pathways [4,5], the abilility of strain waves to transform the macroscopic state of a material has been little explored. Some recent results highlighted the role of volume propagation dynamics in photoinduced processes for different materials exhibiting strongly first order phase transitions without change of symmetry [6-8]. These so-called isosymmetric transitions, similar to the liquid-gas transition, involve totally symmetric electronic and structural changes. In many cases, an isosymmetric Mott IMT, *i.e.* a non-symmetry-breaking electronic and volume change, is coupled to a symmetry breaking ferroelastic transition, *i.e.* a spontaneous lowering of crystalline symmetry associated with shear strain. Hence, the dynamics of both volume and shear strain may contribute to trigger the ultrafast IMT. Providing a comprehensive view allowing to determine the conditions enabling a full dynamical phase transformation at acoustic velocities remains a challenge.

The mechanisms of generation and propagation of photoinduced strain waves in materials are known [9-13]. The coupling of such strain waves with electronic phase transitions, like IMT in Mott materials, poses an altogether new difficulty [7,14]. Namely, the conventional ps acoustics focuses on laser heating of external metallic transducers generating a longitudinal tensile strain wave in a material. By contrast, internal compressive stress in Mott materials are generated by ultrafast electronic photoexcitation of the insulating phase, launching self-supported strain waves from free surfaces. Moreover, sample morphology affects the dynamical strain response [12,15] and may impact the efficiency of strain dynamics on the ultrafast IMT.

Here we investigate the prototypical Mott material V_2O_3, where quantum many body effects between electrons and lattice deformation work cooperatively, and we discuss physical concepts underlying the dynamical strain wave pathway. The relevance of V_2O_3 for exploring this new route stems from its phase diagram at thermal equilibrium (Fig.1a), considered as generic for Mott physics [16]. A first order IMT line separates two isosymmetric paramagnetic phases, PI and PM, with the same rhombohedral space group. Another first-order IMT, between AFI and PM phases, is coupled to antiferromagnetic and monoclinic symmetry breaking. The loss of threefold symmetry axis leads to the formation of ferroelastic domains in the AFI phase [17]. The AFI-PM

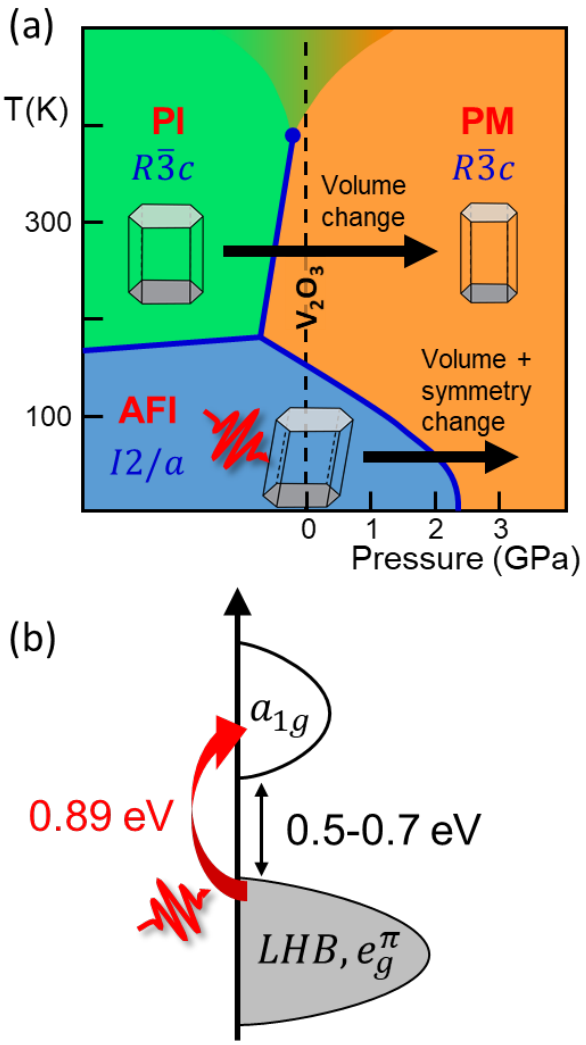

Fig.1 | **Phase Diagram and electronic bandstructure of V_2O_3. (a)** Unit cell symmetry and volume of three phases labelled PI, PM and AFI at thermodynamic equilibrium. Dashed line (vacuum or atmospheric pressure, see text), with cryogenic cooling down to 10 K, for experimental conditions used in this work, *i.e.* far from the AFI-PM transition line. Black arrows underline different nature of transitions, with the isosymmetric PI-to-PM involving only volume change, and the AFI-to-PM involving a fully symmetric volume change, as well as symmetry-breaking structural (ferroelastic to paraelastic) with magnetic changes. **(b)** Schematic representation of DOS in AFI phase; pump laser 0.89 eV close to the bandgap (0.5-0.7 eV) between Lower Hubbard Band (LHB) and the a_{1g} conduction band.

transition is associated with -1.4% volume contraction. Volume and ferroelastic deformations therefore play a conspicuous role in IMT at thermal equilibrium and a central question is how this is reflected in the ultrafast dynamics of IMT.

Different studies have reported ultrafast photoinduced dynamics related with IMT in insulating phases of V_2O_3 by a near-IR pump (1.55 eV) on single crystal [18] or epitaxial films [19-21]. Ref. [18] reports that the transient state from PI to PM results from the electronic excitation to the bonding a_{1g} orbital. In Refs. [19-21], the photoinduced AFI-to-PM dynamics observed close to coexistence regime is discussed in terms of nucleation-growth after ultrafast laser heating. In addition, the observations in Refs. [17,21] disclose a more complex dynamics influenced by the ferroelastic nanotexturing. Finally, intense THz pump pulse is able to induce an ultrafast electronic switching by quantum tunneling, but a slower thermal evolution is observed upon approaching the

AFI-PM transition temperature [22]. The results presented here combine time-resolved (tr) transient reflectivity probing IMT electronic change and X-ray diffraction (XRD) probing structural dynamics after photoexcitation of the AFI phase at similar laser fluences. The chosen experimental conditions limit heating effects thanks to a pump photon energy of 0.89 eV (Fig.1b) close to the optical gap [23-25], and to a base temperature below the AFI-PM coexistence regime to avoid heterogeneous nucleation. The results introduce a mechanism radically different from nucleation-growth, whereby the IMT propagates at sound velocity in the wake of compressive strain wave.

Photoinduced Complete IMT and Reverse Symmetry Breaking in Thin Film

The electronic component of photoinduced IMT is probed by reflectivity change in a 116 nm thick granular film, with a grain size of about 40 nm, 300 ps after photoexcitation at 10 K and at high fluence (7 mJ/cm², Fig.2a,b and Extended Data Fig.1). A broad spectral range is covered, down to the low energies particularly sensitive to metallic state. The photoinduced spectral response matches the differential change in the static reflectivity between the AFI and PM phases, indicating a complete transformation to the metallic phase in the film on this time scale upon strong excitation. In contrast, the photoinduced response of a single crystal shown in Fig.2c,d is significantly lower than its static counterpart, regardless the pump and probe polarisations (Extended Data Fig.2).

The complete photoinduced phase transition in the film is fully confirmed by ultrafast X-ray diffraction obtained on films of comparable (106 nm) and larger (270 nm) thickness, at FemtoMAX for sub-ps time-resolution and at ESRF for high Q-resolution (Methods). Fig.2e,f shows 1D XRD patterns after azimuthal integration of 2D images, measured at 10 K without and with photoexcitation at a fluence inducing complete IMT. Two very clear trends emerge, characterizing the structural transformation from monoclinic AFI phase ($I2/a$ space group) to corundum rhombohedral phase ($R\bar{3}c$ space group). On the one hand, a shift of $(hk0)_H$ Bragg peaks towards large Q is observed, readily visible for $(110)_H$ and $(300)_H$ peaks (we use hereafter the hexagonal notation for clarity, even after splitting of peaks in the monoclinic phase). This demonstrates a photoinduced transient state compressed in the hexagonal (a_H,b_H) plane, in agreement with the structural change at thermal AFI-to-PM phase transition [26] (Extended Data Fig.3).On the other hand, a strong redistribution of intensity occurs on several Bragg peaks, with a narrowing and intensity increase at hexagonal peak position. This corresponds to the disappearance of monoclinic distortion in the AFI phase, particularly unambiguous in the $(116)_H$ Bragg peak, sensitive to ferroelastic shear. These structural changes appear clearly in higher Q-resolution ESRF data shown in Fig.2g-j, with the shift of $(110)_H$ and the merging of three monoclinic peaks into the hexagonal $(116)_H$. A refinement of XRD patterns of initial and completely transformed phases reveals a volume contraction $\Delta V/V$ = -1.5 %, consistent with that at thermal equilibrium, and with a complete reverse ferroelastic symmetry breaking (Extended data Fig.3).

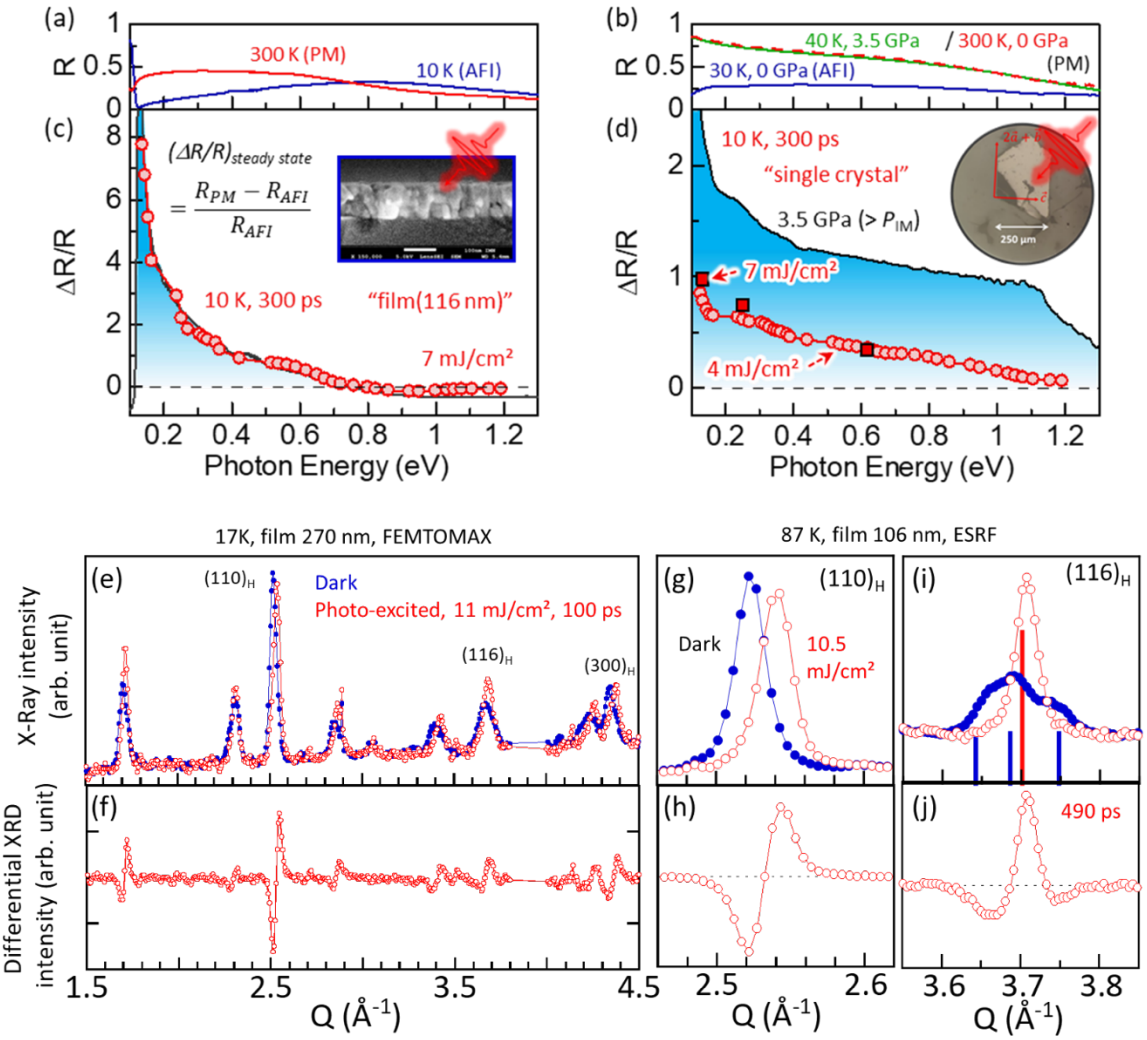

Fig. 2 | Evidence of a complete photoinduced AFI-to-PM phase transition in V_2O_3 granular film and lack thereof in a single crystal. (a) Reflectivity of PM and AFI phases at thermal equilibrium measured on the 116 nm V_2O_3 film. **(c)** Relative difference $\frac{\Delta R}{R} = \frac{R_{PM}-R_{AFI}}{R_{AFI}}$ (blue shaded area) compared to the transient reflectivity change at 300 ps (red dots) measured at 10K over a broad spectral range. No rescaling used, the match of transient reflectivity with that expected of fully converted PM phase is due to applied fluence. Inset: Scanning Electron Microscope cross section image of the film, the reference scale bar (white line) is 100 nm. **(b and d)** same as (**a** and **c**) but for single crystal shown in the inset. In addition, Fig.1b shows similarity between reflectivity at 40 K and 3.5 GPa with reflectivity at 300K and 0 GPa. Polarizations of pump and probe lights are respectively parallel to $2\vec{a}+\vec{b}$ and $\vec{c}$ directions shown in the inset. The difference of reflectivity at thermal equilibrium between the crystal (b) and the thin film (a) results from interference effects between light reflected at the V_2O_3 surface and at the V_2O_3-substrate interface in the film. **(e)** Diffraction pattern of the 270 nm thick film of V_2O_3 at 17K in the ground (Dark) and excited states (100ps delay) with Miller indices on peaks discussed in the text. **(f)** Differential of (e) emphasizing the magnitude of structural change with S/N achieved at Femtomax. **(g)** and **(i)** Bragg reflections $(110)_H$ and $(116)_H$ of the 106 nm thick film at 87 K, bearing predominantly information on volume contraction and symmetry change, respectively, upon AFI to PM transition as measured at ESRF with lower time resolution but improved Q-resolution compared to Femtomax. The peak width and intensity indicate no phase coexistence at 500 ps, and complete transition to PM phase (smaller volume, higher symmetry). Vertical bars in **(i)** are Bragg peak positions and intensities expected in the monoclinic (blue) and hexagonal phases at 300 K (red). **(h)** and **(j)** are the differential of **(g)** and **(i)**, in order to emphasize the magnitude of structural change with S/N achieved at ESRF.

Threshold for the Macroscopic AFI-to-PM Photoinduced Transition

The evolution of transient reflectivity *ΔR/R* with fluence for different time delays gives fundamental information on how the transformation occurs (Fig.3a). For time scales below 1 ps, the increase is quasi-linear in both the thin film and crystal, suggesting an ensemble of independent photoinduced phenomena. In contrast, the thin film shows a non-linear response with fluence after 1 ps with a clear threshold. The occurrence of threshold and amplified nonlinear responsiveness ascertains a photoinduced macroscopic phase transition, as previously evidenced in different materials exhibiting isosymmetric part [6,27,28]. This change of scale from local to macroscopic at the threshold manifests in transient reflectivity also by a loss of coherence of initially in-phase optical phonons [47]. In contrast, the inset of Fig.3a does not reveal any threshold in single crystal. The threshold for IMT in thin film is around 2 mJ/cm^2 at 10 K, and about 1 mJ/cm^2 at 100K (Extended Data Fig.4).

Fig.3b-g shows volume and shear dynamics on the thin film, as extracted from the shift of the $(110)_H$ and the narrowing of the $(116)_H$ Bragg peaks, respectively (Methods and Extended Data Fig. 3 and 6). These tr-XRD results indicate that volume and shear changes also appear above a fluence threshold around 2 mJ.cm^{-2} at 17 K. Moreover,

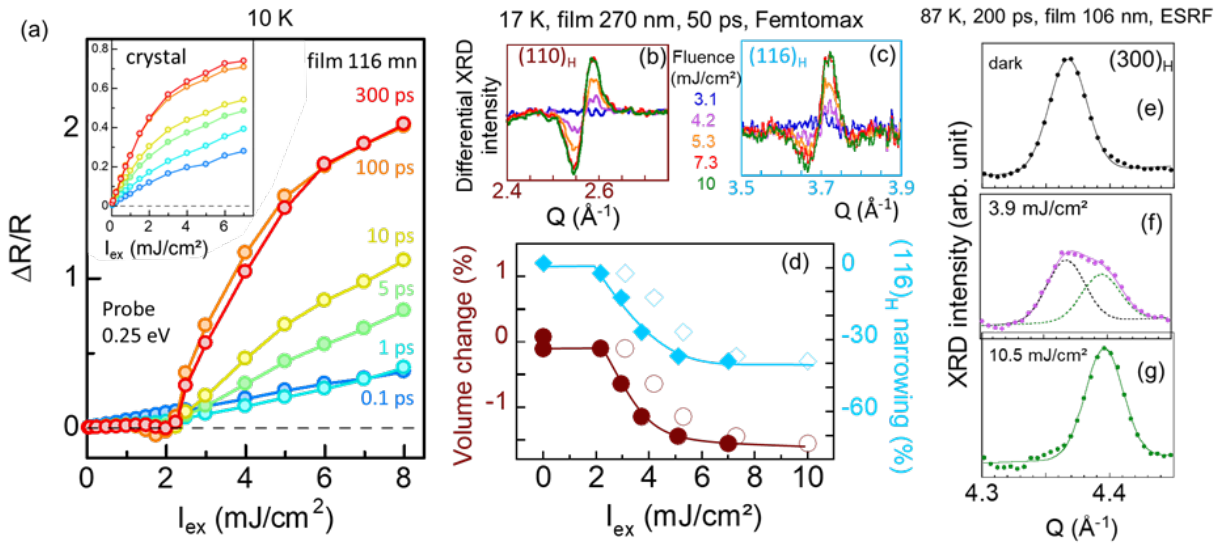

Fig. 3 | Impact of pump laser fluence on the photoinduced electronic and structural features of the AFI-to-PM phase transition. (a) Pump (0.89 eV) laser fluence dependency of transient reflectivity measured at 10 K on a 116 nm V_2O_3 thin film at different delays, probed at 0.25 eV where electronic changes due metallization are most pronounced (Fig.2a). Fluence threshold for the apparent dynamics around around I_{ex} (excitation intensity) = 2 mJ/cm² and delays above 5 ps. Inset: fluence response of V_2O_3 single crystal showing no threshold. **(b)** and **(c)** time-resolved XRD differentials of $(110)_H$ and $(116)_H$ reflections bearing predominantly information on volume contraction and symmetry change, respectively, upon AFI to PM transition measured at 17 K and 50 ps after excitation at varying fluences. **(d)** Evolution with fluence of volume contraction, $(110)_H$ peak shift, and monoclinic to hexagonal symmetry change, $(116)_H$ peak narrowing. The threshold of 2 mJ/cm^2 and saturation around 8-10 mJ/cm^2 are very similar to the values seen in **(a)**. Open symbols correspond to applied laser fluences; filled symbols corrected for different pump incidence angle from **(a)**, see Methods. **(e-g)** Evolution of the $(300)_H$ peak illustrating the phase separation as function of fluence: dark AFI in black (dotted measured, solid fitted), high fluence PM in green (dotted measured, solid fitted), intermediate fluence with phase coexistence in purple (dotted measured, dashed lines AFI and PM peaks fitted).

in the 7-10 mJ.cm^{-2} fluence range, tr-XRD unveil the previously discussed volume contraction of -1.5 % and disappearance of monoclinic distortion, in agreement with the complete IMT probed by tr-reflectivity. At intermediate fluence (3.9 mJ.cm^{-2}, Fig.3f), the observation of distinct Bragg peaks of the initial and photoinduced phases indicates that the partially transformed state corresponds to a phase coexistence between at macroscopic scales.

Driving AFI-to-PM transition by Photoinduced Strain Waves

The temporal signature of strain wave dynamical pathway for IMT directly results from the propagation of photoinduced phase transformation on the acoustic time scale. Fig. 4a,b and Extended Data Fig. 5 show the evolution of the symmetry and volume changes in two granular films of different thickness (106 and 270 nm) but similar grain size. These evolutions are extracted from the narrowing of the $(116)_H$ and the shift of the $(110)_H$ Bragg peaks, respectively (Methods). However, a whole pattern refinement was also performed on the thinnest film (Extended Data Fig. 6), and lead to the same conclusion. Whereas the monoclinic to hexagonal transition is completed in less than 3 ps, the volume contraction requires longer time and shows an onset of around 9 ps. Unlike the dynamics of symmetry change, the time for volume contraction scales with the film thickness. Indeed, from the onset to the end of propagation, this time is 16 and 40 ps in the 106 and 270 nm films, respectively.

These shear and volume dynamics can be rationalised with strain waves scenario with two components, a shear one and a volumic one propagating on different length scales. Since the average size of ferroelastic domain is around 20 nm (Extended Data Fig. 1e), the observed shear acoustic time scale agrees with a propagation time of 2.5 ps at transverse acoustic velocity of 4 nm/ps [29-31] from two opposite faces of the domain towards its centre (Fig.5). Similarly, the expected propagation times for a longitudinal strain wave through the film at the reported acoustic velocity of 7-7.3 nm/ps [29-31] are 15 and 38 ps for the 106 and 270 nm, respectively, in agreement with the experimental values shown in Fig.4b.

Remarkably, transient reflectivity follows closely the structural dynamics (Fig.4): a fast increase during the first ps is followed by a linear increase, concurrently with the propagation of the volume on the acoustic time scale. According to tr-XRD, V_2O_3 reaches the $R\bar{3}c$ symmetry after 3 ps with volume unchanged, hence resembling the PI phase shown in Fig.1. Since the PI phase has reflectivity greater than AFI [32], a fast reflectivity increase is expected on few ps. At longer delays, the AFI-to-PM dynamics of both tr-reflectivity and tr-XRD end in a long-lived transient state. A noteworthy feature is that the dynamical time scale is essentially the same regardless the laser fluence above the threshold and the base temperature. At intermediate fluence, the smaller reflectivity change agrees with the phase coexistence discussed above (Fig. 3f).

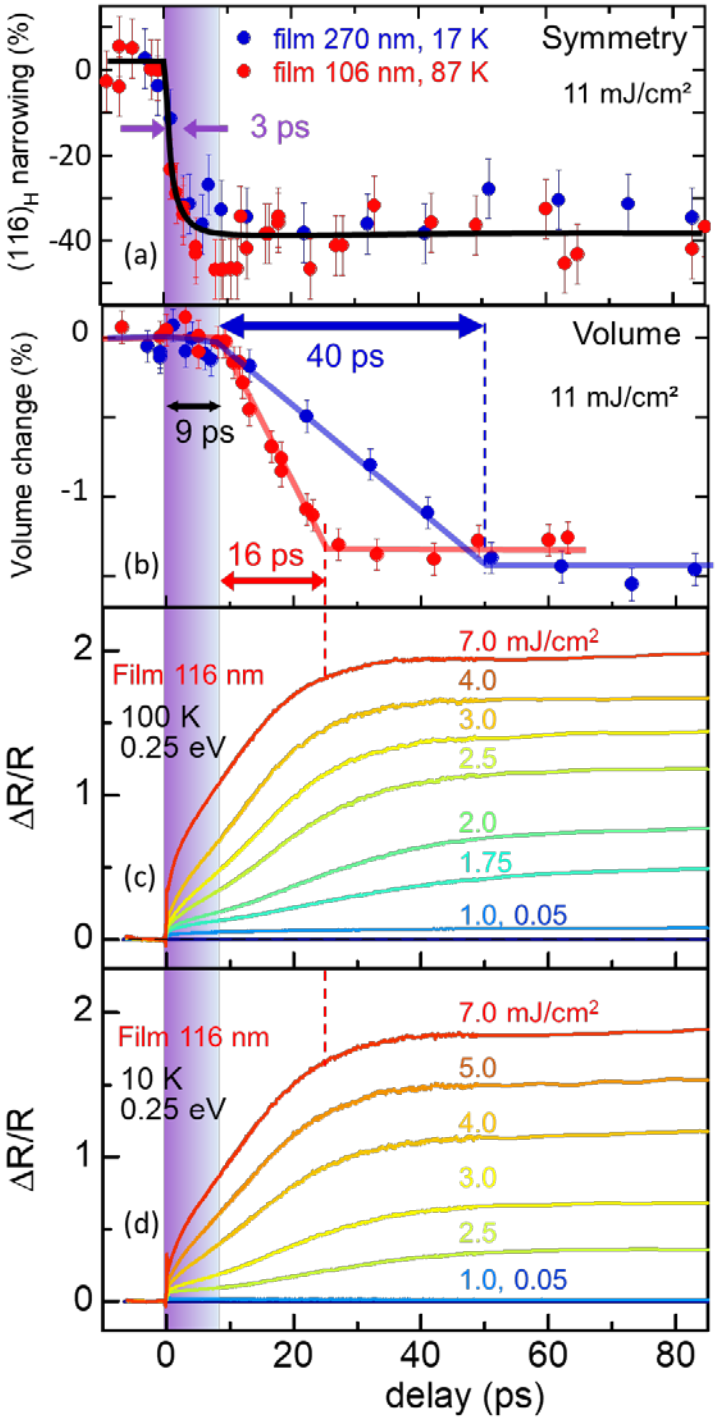

Fig. 4 | Structural and electronic changes on the acoustic time-scales. (a) Evolution of photoinduced symmetry change probed by $(116)_H$ peak narrowing in 106 nm (red) and 270 nm (blue) films at 87 K and 17 K, respectively. The signal rises in less than 3 ps, after time binning over 1 ps with jitter corrected. **(b)** Evolution of volume change probed by the $(110)_H$ Bragg peak shift (see Extended Data Fig.3). Apparent incubation time of 9 ps (indicated by the purple shade stripe) is followed by a linear decrease of average volume of 16 ps for 106 nm, and 40 ps for 270 nm films. Colour coding as in (a), but time binning of 2 ps. The curves in (a) and (b) are guides for the eyes. **(c)** and **(d)** transient reflectivity of the 116 nm film excited with different fluences at 100K and 10K, respectively. The linear evolution of transient reflectivity coincides temporally with the onset of 9 ps seen in tr-XRD (shaded area) and the end of volume contraction 16 ps later (dashed red line).

Finally, the recovery of the initial state in thermal equilibrium with its environment takes place on longer time scale, typically longer than 1 ns (Extended Data Fig. 9).

Physical Picture and Outlook

Symmetry and cooperativity

The observation of successive reverse ferroelastic and insulator-to-metal transitions (schematically illustrated in Fig.5) highlights the fundamental difference between symmetry-breaking and isosymmetric phase transition dynamics. At thermal equilibrium, the nature of these two kinds of phase transitions is distinct [33]. Spontaneous symmetry-breaking occurs on the phase coexistence line below the transition temperature at zero conjugated field. This manifests by the emergence of domains due to the loss of symmetry elements. Conversely, an isosymmetric phase transition, like the liquid-gas or Mott transition [34], occurs by crossing of a phase coexistence line by varying a thermodynamic control parameter (temperature T, pressure P). It usually involves large discontinuities of entropy and volume, characteristic of strongly first order nature. In such isosymmetric transitions, a metastability regime emerges in the free energy landscape between spinodal limits [33,35]. In many quantum materials, like V_2O_3, an isosymmetric Mott transition is coupled with a symmetry-breaking ferroic ordering. A non-equilibrium potential energy landscape controlled by laser fluence may be considered to determine the macroscopic stable state attained at the end of the photoinduced process [5]. For the coherent structural dynamics, the potential energy governing the new atomic equilibrium positions is determined by the new (photoinduced) electronic subsystem. Moreover, a difference between a reverse symmetry-breaking and isosymmetric processes may be reflected in the dynamics given the existence of two length scales, namely the domain size and the film thickness. A two-step transition dynamics is indeed observed (Fig.4). The shear dynamics for reverse ferroelastic transition, scaling temporally with the small domain size, is faster than the volume dynamics scaling with the much larger film thickness, despite a smaller acoustic velocity for the shear waves. This contrasts with the main assumption of [8] that symmetry broken domains, such as ferroelastic ones, slow down the photoinduced insulator-metal transition Mott transition.

At thermal equilibrium, cooperative interactions act as an internal mean field providing positive feedback upon crossing the phase coexistence line of isosymmetric phase transition. Positive cooperative feedback should play a role in the photoinduced phase transitions. For example, in a theoretical study on V_2O_3 based on a two orbital model, the excess population of electrons in the upper orbital and holes in lower orbital may cause a gap collapse at a threshold value of population through such feedback effect [36]. Similarly, the long range elastic interactions can also stimulate a cooperative response, for instance when photoinduced compressive stress can generate an effective positive chemical pressure [37]. The chemical pressure increases proportionally with the number of excited electrons, hence behaving as an internal mean field enhancing the transformation to a low volume phase synergetically with electronic Mott physics. In other words, this active role of volume results from the existence of an isosymmetric phase transition, whether or not coupled to a symmetry breaking, at thermal equilibrium or during dynamical process. In contrast, the volume

is not significantly affected during the dynamical transition to paraelastic state, in agreement with its secondary role in any symmetry-breaking instability.

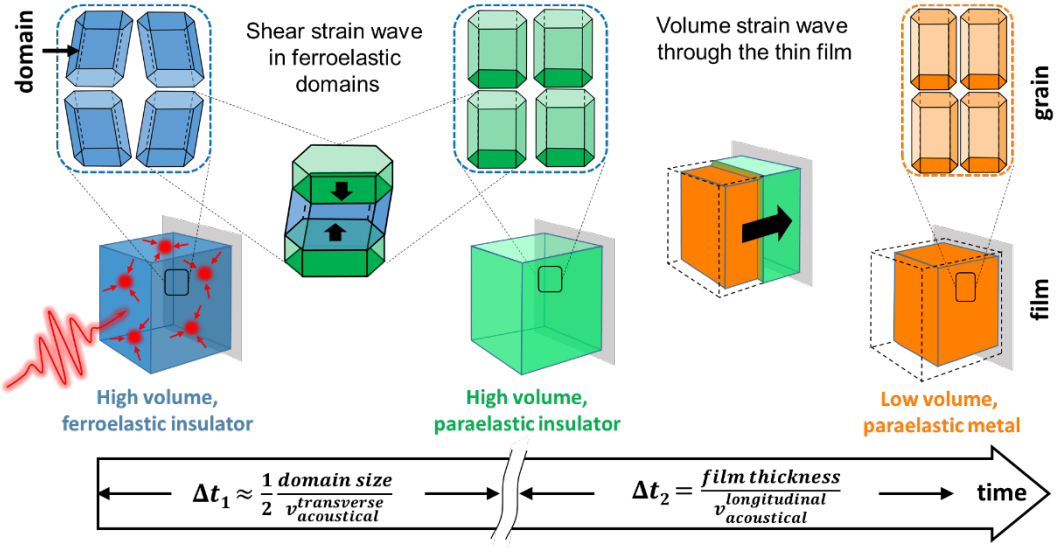

Fig. 5 | Schematic illustrating the photoinduced strain waves driving the AFI-to-PM transition in granular thin film of V_2O_3. Ultrafast laser pulse excites long-lived electronic precursors, leading to fast build-up of shear and volume mechanical stress. At first, the stress is relaxed by launching a shear strain wave within each ferroelastic domain of the granular film, Δt_1. Then a compressive volume strain wave propagates from free surface of the film towards the substrate, leaving in its wake the insulator to metal transition, Δt_2.

Strain-wave physics and morphology

Our experimental work underlines the importance to consider the often neglected physics of strain-waves. Firstly, we can mention that a volume contraction is generated through a deformation potential related with internal modification of electronic distribution [11]. Not only photoexcited electronic states can persist after ultrafast intraband relaxation before recombination, but their lifetime may be extended by self-trapping [38] implying local structural distortions of V_2O_3 units, such as small polarons [39]. This could be the situation in V_2O_3, since long-lived transient states are observed at low fluence (Extended Data Fig.7). In order to recover mechanical equilibrium with external pressure, longitudinal strain waves are launched from the surface, involving long wavelength acoustic phonons (typically twice the film thickness or laser penetration, [12]) leaving in its wake a long lasting deformation with contracted volume. As stated in [13], the coherent 1D strain wave propagating through the film also holds for spatially homogeneous photoexcitation, which is quite different from the 2D in-plane thermal nucleation and growth proposed in the Avrami picture [19]. Unlike the longitudinal strain waves, there is no clear theoretical description for generating the shear waves. However, it is fair to expect that shear waves are launched at the domain walls as the initial location of mechanical non-equilibrium for shear process.

An important consequence of the strain wave mechanism is the crucial role played by morphology on the efficiency of the photoinduced phase transitions. The absence of

threshold in single crystal and a response smaller than expected for a complete AFI-to-PM transition are consistent with a strain wave picture. Single crystal indeed constitutes a continuous medium where only transient longitudinal deformation propagates unimpeded in the direction perpendicular to the film's surface and with clamped transverse deformations [12,15] hindering a complete volume change. This situation is avoided in granular films, where the volume of each grain is essentially free to deform in all directions on a similar time-scale. For this reason the results on epitaxial films should be interpreted with some caution as the ability to deform might be restricted compared to granular polycrystalline films. Moreover, ferroelastic domains may be significantly larger in single crystal or epitaxial films, therefore significantly prolonging the time scale for shear dynamics. Thus, pre-existing large monoclinic domains persist after photoexcitation of epitaxial V_2O_3, possibly hindering the ultrafast transformation to metallic phase [17]. This highlights that controlling the domain sizes is a key factor for propagating IMT at sound velocity.

Our study also unveiled an intriguing feature, namely the observation of a delayed onset for the volume dynamics. At this stage it is difficult to give a satisfying explanation. We may only mention a possible relation with the granular nature of thin film, known to affect the longitudinal strain response [12,15,40], as well as slowing down of the initial volume dynamics resulting from its coupling with shear dynamics [41].

Finally, we would like to stress that the photoinduced effects discussed here are transient, *i.e.* they are volatile and relax within 1-100 ns (Extended Data Fig. 9). From this perspective, the description of long-lived hidden quantum state [42] or non-volatile electrically-driven ones [43] have another physical underpinning and most probably call for elasticity beyond linear regime [44].

To conclude, this work reports a complete set of novel experimental evidence in a generic Mott insulator, bringing to light key features for the understanding of a universal physical picture of ultrafast strain wave pathway in quantum materials. A key observation is that a photoinduced insulator–to-metal transition occurs in V_2O_3, but only in the wake of a compressive strain wave. This indicates that the change in macroscopic electronic behavior only happens when the volume has changed. The findings provide new perspective on the role of elastic deformation propagation in ultrafast phase transitions. The isosymmetric and symmetry breaking dynamics are clearly differentiated and the active role of volume for Mott cooperativity highlighted. The clear impact of morphology on the efficiency of dynamical processes emphasizes the importance of the physics of strain wave propagation. The concepts discussed here are applicable to any material exhibiting isosymmetric transitions, whether coupled or not to symmetry breaking. A good example is mixed-stack charge transfer complex where an isosymmetric phase transition between neutral band insulator and ionic Mott insulator is coupled to a ferroelectric symmetry-breaking [27,45,46]. A similar situation occurs in other classes of materials involving a ferroelastic symmetry breaking driven by a Jahn-Teller distortion, such as Prussian blue analogs [47,48]. In other more complex examples, such as Mott-Peierls insulators like VO_2 [49] or 1T-TaS_2 [40], the

physical picture offered here may help solve the respective contributions of isosymmetric (Mott) and symmetry-breaking (charge density wave/Peierls) to the ultrafast dynamics. The outreach may include topological isosymmetric transitions, in which elastic interactions are equally important, for instance a Lifshitz transition with giant lattice softening [50]. This work may stimulate further theoretical developments and also guide the assessment of the ultimate performance of ultrafast memristive devices based on Mott insulators [51,52].

References:

1 Huber, T. et al. Coherent structural dynamics of a prototypical charge-density-wave-to-metal transition. *Physical Review Letters* **113**, 026401 (2014). doi: 10.1103/PhysRevLett.113.026401

2 Teitelbaum, S. W. et al. Real-time observation of a coherent lattice transformation into a high-symmetry phase. *Physical Review X* **5**, 031081 (2018). doi: 10.1103/PhysRevX.8.031081

3 Trigo, M. et al. Coherent order parameter dynamics in $SmTe_3$. *Physical Review B* **99**, 104111 (2019). doi: 10.1103/PhysRevB.99.104111

4 Basov, D. N., Averitt, R. D. & Hsieh, D. Towards properties on demand in quantum materials. *Nature Materials* **6**, 1077 (2017). doi: 10.1038/nmat5017

5 De la Torre, A., et al. Nonthermal pathways to ultrafast control in quantum materials. *Reviews of Modern Physics* **93**, 041002 (2021). doi: 10.1103/RevModPhys.93.041002

6 Bertoni, R. *et al.* Elastically driven cooperative response of a molecular material impacted by a laser pulse. *Nature Materials* **15**, 606 (2016). doi: 10.1038/nmat4606

7 Mariette, C. *et al.* Strain wave pathway to semiconductor-to-metal transition revealed by time-resolved X-ray powder diffraction. *Nature Communications* **12**, 1239 (2021). doi: 10.1038/s41467-021-21316-y

8 Verma, A. *et al.* Picosecond volume expansion drives a later-time insulator-metal transition in a nano-Textured Mott insulator. *Nature Physics* (2024). doi.org/10.1038/s41567-024-02396-1

9 Thomsen, C., Grahn, H. T., Maris, H.J. & Tauc, J. Surface generation and detection of phonons by picosecond light pulse. *Physical Review B* **34**, 4129 (1986). doi: 10.1103/PhysRevB.34.4129

10 Matsuda, O., Larciprete, M. C., Li Voti, R. & Wright, O. B. Fundamentals of picosecond laser ultrasonics. *Ultrasonics* **56**, 3 (2015). doi: 10.1016/j.ultras.2014.06.005

11 Ruello, P. & Gusev, V. E. Physical mechanisms of coherent acoustic phonons generation by ultrafast laser action. *Ultrasonics* **56**, 21 (2015). doi: 10.1016/j.ultras.2014.06.004

12 Mattern, M. et al. Concepts and use cases for picosecond ultrasonics by x-rays. *Photoacoustics* **31**, 100503 (2023). doi: 10.1016/j.pacs.2023.100503

13 Schick, D. et al. Ultrafast lattice response of photoexcited thin films studied by X-ray diffraction. *Structural Dynamics* **1**, 064501 (2014). doi: 10.1063/1.4901228
14 Okimoto, Y. et al. Ultrasonic propagation of metallic domain in $Pr_{0.5}Ca_{0.5}CoO_3$ undergoing a photoinduced Insulator-to-Metal Transition. *Physical Review Letters* **103**, 027402 (2009). doi: 10.1103/PhysRevLett.103.027402
15 Von Reppert, A. et al. Ultrafast laser generated strain in granular and continuous FePt thin films. *Applied Physics Letters* **113**, 123101 (2018). doi: 10.1063/1.5050234
16 McWhan, D. B. et al. Electronic specific heat of metallic Ti-doped V_2O_3. *Physical Review Letters* **27**, 941 (1971). doi: 10.1103/PhysRevLett.27.941
17 Ronchi, A. *et al.* Nanoscale self-organization and metastable metallicity in Mott insulators. *Nature Communications* **13**, 3730 (2022). doi: 10.1038/s41467-022-31298-0
18 Lanz, G. *et al.* Ultrafast evolution and transient phases of prototype out-of-equilibrium Mott-Hubbard material. *Nature Communications* **8**, 13917 (2017). doi: 10.1038/ncomms13917
19 Abreu, E. *et al.* Dynamic conductivity scaling in photoexcited V_2O_3. Thin Films. *Physical Review B* **92**, 085130 (2015). doi: 10.1103/PhysRevB.92.085130
20 Singer, A. *et al.* Nonequilibrium phase precursors during a photoexcited insulator-to-metal transition in V_2O_3. *Physical Review Letters* **120**, 207601 (2018). doi: 10.1103/PhysRevLett.120.207601
21 Ronchi, A. *et al.* Early-stage dynamics of metallic droplets embedded in nanotextured Mott insulating phase of V_2O_3. *Physical Review B* **100**, 075111 (2019). doi: 10.1103/PhysRevB.100.075111
22 Giorgianni, F. *et al.* Overcoming the thermal regime for the electric-field driven Mott transition in vanadium sesquioxyde. *Nature Communications* **10**, 1159 (2019). doi: 10.1038/s41467-019-09137-6
23 Thomas, G. A. *et al.* Observation of the gap and kinetic energy in a correlated insulator. *Physical Review Letters* **73**, 1529 (1994). doi: 10.1103/PhysRevLett.73.1529
24 Baldassare, L. *et al.* Quasiparticle evolution and pseudogap formation in V_2O_3: an infrared spectroscopy study. *Physical Review B* **77**, 113107 (2008). doi: 10.1103/PhysRevB.77.113107
25 Stewart, M. K. *et al.* Insulator-to-metal transition and correlated metallic state of V_2O_3 investigated by optical spectroscopy. *Physical Review B* **85**, 205113 (2012). doi: 10.1103/PhysRevB.85.205113
26 McWhan, D. B. & Remeika, J. P. Metal-Insulator transition in $(V_{1-x}Cr_x)_2O_3$. *Physical Review B* **2**, 3734 (1970). doi: 10.1103/PhysRevB.2.3734
27 Iwai, S. *et al.* Ultrafast optical switching from a ionic to neutral state in tetrathiafulvalrne-p-chloranil (TTF-CA) observed in femtosecond reflection

spectroscopy. *Physical Review Letters* **88**, 057402 (2002).
doi: 10.1103/PhysRevLett.88.057402

28 Wall, S. *et al.* Ultrafast disordering of vanadium dimers of photoexcited VO_2. *Science* **362**, 572 (2018).
doi: 10.1126/science.aau3873

29 Motin Seikh, Md. *et al.* A Brillouin study of the temperature-dependences of the acoustic modes across the insulator-metal transitions in V_2O_3 and Cr-doped V_2O_3. *Solid State Communications* **138**, 466 (2006).
doi: 10.1016/j.ssc.2006.03.026

30 Yelon, W. B. & Keem, J. E. The elastic constants of V_2O_3 in the insulating phase. *Solid State Communications* **29**, 775 (1979).
doi: 10.1016/0038-1098(79)90159-5

31 Yethiraj, M., Werner, S.A., Yelon, W.B. & Honig, J. M. Phonon anomalies and the magnetic transition in pure and Cr-doped V_2O_3. *Physical Review B* **36**, 8675 (1987).
doi: 10.1103/PhysRevB.36.8675

32 Lo Vecchio, I. *et al.* Optical properties of V_2O_3 in its whole phase diagram. *Physical Review B* **91**, 155133 (2015).
doi: 10.1103/PhysRevB.91.155133

33 Chaikin, P. M. & Lubensky, T. C. *Principles of condensed matter physics* (Cambridge University Press, 1995)

34 Georges, A., Florens, S. & Costi, T. A. The Mott transition: Unconventional transport, spectral weight transfers, and critical behaviour. *J. Phys. IV France* **114**, 165–173 (2004).
doi: 10.1051/jp4:2004114040

35 Chernyshov, D., Bürgi, H.-B., Hostettler, M. & Törnroos, K. W. Landau theory for spin transition and ordering phenomena in Fe(II) compounds. *Phys. Rev. B* **70**, 094116 (2004)

36 Sandri, M. & Fabrizio, M. Nonequilibrium gap collapse near a first-order Mott transition. *Physical Review B* **91**, 115102 (2015).
doi: 10.1103/PhysRevB.91.115102

37 Spiering, H., Boukheddaden, K., Linares, J. & Varret, F. Total free energy of a spin-crossover molecular system. *Physical Review B* **70**, 184106 (2004).
doi: 10.1103/PhysRevB.70.184106

38 Nasu, K. Real time quantum dynamics of spontaneous translational symmetry breaking in the early stage of photo-induced structural phase transitions. *Applied Science* **8**, 332 (2018).
doi: 10.3390/app8030332

39 Wickramane, D., Bernstein, N. & Mazin, I. I. Role of defects in the metal-insulator transition in VO_2 and V_2O_3. *Physical Review B* **99**, 214103 (2019).
doi: 10.1103/PhysRevB.99.214103

40 Reid, A.H. *et al.* Beyond a phenomenological description of magnetostriction. *Nature Communications* **9**, 388 (2018).
doi: 10.1038/s41467-017-02730-7

41 Li, J. *et al.* Probing the pathway of an ultrafast structural phase transition to illuminate the transition mechanism in Cu_2S. *Applied Physics Letters* **113**, 041904

(2018).
doi: 10.1063/1.5032132
42 Stojchevska L. *et al.* Ultrafast switching to a stable hidden quantum state in an electronic crystal Science 344, 177 (2014).
doi: 101126/science.1241591
43 Janod, E. *et al.* Resistive Switching in Mott Insulators and Correlated Systems. Advanced Functional Materials 25, 6287–6305 (2015).
10.1002/adfm.201500823
44 van Capel, P. J. S., Péronne, E. & Dijkhuis, J. I. Nonlinear ultrafast acoustics at the nano scale. *Ultrasonics* **56**, 36–51 (2015).
doi: 10.1016/j.ultras.2014.09.021 10.1016/j.ultras.2014.09.021
45 Lemée-Cailleau, M.H. *et al.* Thermodynamics of the neutral-to-ionic transition as condensation and crystallization of charge-transfer excitations *Physical Review Letters* **79**, 790 (1997).
doi: 10.1103/PhysRevLett.79.1690c
46 Takehara, R. *et al.* Revisited phase diagram on charge instability and lattice symmetry breaking in the organic ferroelectric TTF-QCl_4. *Phys. Rev. B* **98**, 054103 (2018).
doi.org/10.1103/PhysRevB.98.054103
47 Azzolina, G. *et al.* Landau theory for non symmetry-breaking electronic instability coupled to symmetry-breaking order parameter applied to Prussian blue analog *Physical Review B* **102**, 134104 (2020).
doi: 10.1103/PhysRevB.102.134104
48 Azzolina, G. *et al.* Out-of-equilibium response to photo-induced charge transfer in a MnFe Prussian blue analog Journal of Materials Chemistry C **9**, 6773 (2021).
doi: 10.1039/d1tc01487k
49 Nájera, Ó., Civelli, M., Dobrosavljević, V. & Rozenberg, M. J. Resolving the VO_2 controversy: Mott mechanism dominates the insulator-to-metal transition. *Physical Review B* **95**, (2017).
doi : 10.1103/PhysRevB.95.035113
50 Noad H.M.L. Giant lattice softening at a Lifshitz transition in Sr_2RuO_4. *Science* **382**, 447 (2023).
doi: 101126/science.adf3348
51 Sood, A. *et al.* Universal phase dynamics in VO_2 switches revealed by ultrafast operando diffraction. *Science* **373**, 352 (2021).
doi: 10.1126/science.abc0652
52 Cario, L., Tranchant, J., Corraze, B. & Janod, E. Chapter 10 - Correlated transition metal oxides and chalcogenides for Mott memories and neuromorphic applications. in *Metal Oxides for Non-volatile Memory* (eds. Dimitrakis, P., Valov, I. & Tappertzhofen, S.) 307–360 (Elsevier, 2022).
doi: 10.1016/B978-0-12-814629-3.00010-6.

Methods

Materials synthesis and characterization

V_2O_3 single crystals were obtained by introducing 500 mg of V_2O_3 powder - previously prepared by reducing V_2O_5 (Aldrich, >99.6%) at 900 °C for 10 h under a Ar 95% / H_2 5% gas flow - in a silica tube, along with 40 mg of sulfur as a vapor phase transport agent. The tube was vacuum sealed, heated up to 1050 °C in a temperature gradient (≈10 °C/cm) furnace, and then cooled down at −2 °C/h to 900 °C, before a faster cooling (−300 °C/h) to room temperature. This treatment resulted in a high yield of V_2O_3 single crystals of typical size 300-500 µm.

Thin film of V_2O_3 were deposited by reactive sputtering of V targets in Ar 95% / O_2 5% discharge [51] on (0001)-oriented sapphire substrates. Post deposition annealing at 530°C in a reducing Ar 95 % / H_2 5% gas flow yields a granular, polycrystalline and single-phased V_2O_3 film, as evidenced in Extended Data Fig. 1. The typical domain size, estimated by analyzing the width of X-ray diffraction Bragg peaks with the Scherrer formula gives 40 nm at room temperature in the hexagonal $R\bar{3}c$ phase and 20 ± 5 nm at 87 K in the monoclinic $I2/a$ phase. The domain size at room temperature is consistent with the average grain size observed by Scanning Electron Microscopy (Extended Data Fig. 1). The significant decrease of the domains size in the monoclinic phase indicates that each single-domain grain at room temperature splits on average into a few domains at the hexagonal $R\bar{3}c$ to monoclinic $I2/a$ transition.

Resistivity *vs* temperature curves displayed in Extended Data Fig. 1d allow detecting typical insulator to metal transition temperatures around 160 K upon heating in the single crystal, as expected for stoichiometric V_2O_3 [25]. Transition temperature above 135 K involving a 10^5 increase of resistivity in the films indicate a composition very close to stoichiometry.

Finally, let us mention that evaluating in a reliable way the penetration depth at 0.89 eV of the pump laser used in this study is not an easy task. Estimates based on published data on reflectivity [32,52,53] or ellipsometry data [54] leads to penetration depths at 0.89 eV varying between 150 nm [54] and 800 nm [52]. Our own measurements, evaluated from the reflectivity and transmittance of thin films in the AFI phase, give a slightly narrower estimate, in the 200-400 nm range. This ensures a substantial photoexcitation of the V_2O_3 films used in this work (thickness from 100 nm to 270 nm) up to the substrate.

Transient reflectivity measurements

For optical pump-probe spectroscopy for measuring transient reflectivity ($\Delta R/R$) spectra, the fundamental output from a Ti: Sapphire regenerative amplifier, operating at 1 kHz, 800 nm, with a pulse width of *ca*. 100 fs, was used for the excitation of optical parametric amplifiers (OPAs). Wavelength of an OPA for pump beam was set at 1400 nm (0.89 eV), whereas another OPA is used for probe beam covering the spectral range between 1000 -12000 nm (0.1 -1.2 eV). The probe beam was focused on the center of the pumping area on the sample which is set in the conduction-type liquid-He cryostat. Polarization directions of pump and probe beams are normal to each

other.The diameters of pumping and probing areas are 400-500 micron and 100-200 micron, respectively. Then the reflected beam from the sample was detected by an InGaAs (1000-2200 nm) or a HgCdTe (2500-10000 nm) photodetector after passing through a monochromator. The pump-on and pump-off were alternately switched by the feed-back-controlled optical chopper, synchronized with the 1 kHz laser driver. Each probe shot was sampled using boxcar integrators. After normalization by a reference pulse, the observed intensity of respective shots was recorded in the PC to calculate $\Delta R/R$. Time resolution is 150-200 fs depending on the probing wavelength.

Ultrafast X-ray diffraction

1- FEMTOMAX

Experimental set-up

The sub-picosecond time-resolved X-Ray diffraction experiment was carried out at the FemtoMAX beamline at MAX IV Laboratory in Sweden. The sample was placed in the GIXS endstation operated at ultrahigh vacuum < 10^{-7} mbar and equipped with the JANIS ST-400 UHV supertran cryostat allowing for a broad temperature range (10 – 500 K) of sample temperatures. The sample temperature was monitored using a DT-670B silicon diode mounted next to a sample and a standard temperature controller (Model 335) from the Lake Shore Cryotronics, Inc. 100 fs long X-ray pulses delivered at 10 Hz with tunable energy around 9 keV was used for the experiment. A double multilayer monochromator with the 2 % bandwidth delivered by Rigaku was used to select the X-ray energy. The X-ray spot size on sample, tilted by 6 deg from grazing incidence, was 60 × 570 μm^2 (FWHM). X-ray scattering was carried out in a forward geometry. X-rays scattered from the V_2O_3 sample were collected using a Pilatus time over threshold detector from Dectris, mounted at a distance of 12 cm from the sample at an angle of 30º. The highest scattering vector giving acceptable resolution was Q = 4.5 $Å^{-1}$.

Laser system and synchronisation

The 1300 nm central wavelength laser pump pulse was generated from in an OPA (HE-TOPAS, Light Conversion). The beam was incident on the sample at an angle of 23 degrees relative to the sample surface with either s-polarization (yielding a reflecticity at the film surface $R \approx 0.5$) or p-polarization ($R \approx 0$). The footprint was 300 µm (FWHM, lateral) and 2.8 mm (FWHM, longitudinal). The maximum peak fluence under these conditions was 60 mJ/cm^2. As only 50 % of incident fluences measured with s-polarization is transmitted to the film, such as in Fig.2d, the tr-XRD fluences need to be rescaled by a factor of ≈ 0.70 to be compared with transient reflectivity ones obtained in normal incidence with 75 % of incident light transmitted to the film. The synchronization between the laser and x-ray pulse was managed by electronically phase locking the Ti:Sapphire mode-locked laser, to the reference RF signal, used in the LINAC, utilizing a standard locking scheme. Pump/probe jitter and drifts of each shot was recorded using a monitor developed at the FemtoMAX beamline. This pump/probe delay monitor extracts its reading from signals derived from a fast photo diode, for the laser pulse, and a pickup antenna at the electron bunch transport tube after the FemtoMAX undulator pair. The two signals are combined and in turn excites

a broadband RF cavity band pass filter. The resulting ringing signal pair is digitally sampled and processed by an algorithm that extracts the delay from the relative phases of the signal pair. The accuracy of this pump/probe delay monitor has been tested to be 210 fs (FWHM).

2- ESRF

X-ray diffraction experiment at ESRF, ID09 beamline, was performed during hybrid mode (24x8 multiple electron bunches + 1 single bunch). The single electron bunch (8 mA) was used in the experiment. The ID09 setup was discussed in detail previously [55]. Briefly, a fast rotating chopper was used to isolate X-ray single pulses (each < 100 ps long) at 1 kHz repetition rate. The X-rays energy was centered at 15 keV. Cryogenically cooled Si(111) monochromator was used to reduce the x-ray bandwidth ($\Delta E/E = 10^{-4}$) in order to optimize the Q-resolution. The measurements were taken in reflection geometry with a fixed incident angle of 6 degrees. In this geometry, the X-ray footprint on the sample was 50 (horizontal) × 250 (vertical) μm^2. Diffracted images were collected on a Rayonix MX170-HS CCD detector (sample to detector distance = 150 mm).

A synchronized Ti:Sapphire laser with 1.5 ps pulse duration was used to photo-excite the sample. The 1300 nm pump wavelength was obtained using an OPA (TOPAS, LightConversion). Laser was hitting the sample from the top, perpendicular to x-rays, and focused to accommodate the elongated x-ray footprint. Spot size on sample was 1.17 mm (along x-ray direction) * 0.33 mm.

Measurements were taken in stroboscopic mode and each image was recorded with 10^3 shots exposures. “Negative” delays, for which x-ray arrive before photo-excitation, were interleaved as references. The delay sequences were repeated several times to increase the signal to noise ratio on differential patterns.

The sample was mounted on the cold finger of a specially designed continuous N_2-flow cryostat with Mylar windows for transmission of incident and diffracted 15 keV x-rays, and a UV-fused silica window for pump laser transmission.

X-Rays Diffraction data reduction

The azimuthal integration was performed using the pyFAI python library. The sample and beamstop holder shadows were masked. The effective azimuthal range used for the integration was +/-70 degrees and +/- 60 degrees (for ID09 and Femtomax data respectively, see Extended Data Fig.8). This range is defined around the plane containing the direction normal to the sample surface (the plane was vertical in the two experiments).

Refinement of Femtomax 1D patterns

Individual peak fitting was performed on the 1D patterns. Both (110) and (116) Bragg peaks were refined using a single pseudo-voigt with a linear background.

$$I = (1-\Gamma).A.exp\left(\frac{(x-x_0)^2}{2\sigma^2}\right) + \Gamma.A.\frac{\sigma^2}{(x-x_0)^2+\sigma^2} + y_0 + y_1.x$$

The gaussian/lorentzian ratio Γ was refined against one reference pattern with no laser and then kept fixed. This ration was found equal to 0.3. Background parameters y_0 and y_1, amplitude A, center x_0 and width σ were free parameters. The full width half maximum was calculated as follow:

$$FWHM = 2\sigma\sqrt{2.ln2)}$$

The volume change was estimated by calculating the peak shift between the time delay and the closest reference with no laser. This procedure allowed for accounting for the drifts in sample to detector distance.

$$\frac{\Delta V_t}{V} = 2\,\frac{\Delta a_{H,t}}{a_H} = -2\,\frac{x_{0,t} - x_{0,ref}}{x_{0,ref}}$$

Similarly the narrowing of the $(116)_H$ Bragg peak was estimated as follow:

$$\frac{\Delta FWHM_t}{FWHM} = \frac{\mathrm{FWHM}_{0,t} - \mathrm{FWHM}_{0,ref}}{\mathrm{FWHM}_{0,ref}}$$

The validity of this approach is further discussed in Extended Data Fig.3 and 6.

Refinement of ID09 1D patterns

Individual peak fitting was performed on the 1D patterns in order to estimate the amount of AFI / PM phases. In this case the peaks of the two phases could be distinguished. The $(110)_H$ peak was thus refined using two gaussian peaks of identical width with linear background.

$$I = (1-\Gamma).A.exp\left(\frac{(x-x_0)^2}{2\sigma^2}\right) + \Gamma.A.\frac{\sigma^2}{(x-x_0)^2+\sigma^2} + y_0 + y_1.x$$

The ratio R between AFI and PM phase was calculated as the ratio between the two peaks integral:

$$R = \frac{FWHM_1.A_1}{FWHM_0.A_0 + FWHM_1.A_1} = \frac{\sigma.A_1}{\sigma.A_0 + \sigma.A_1} = \frac{A_1}{A_0 + A_1}$$

Reflectivity under pressure

Low temperature pressure-dependent optical conductivity spectra have been deduced from nearly normal incidence sample-diamond reflectivity R_{sd} (ω) between 550 and

12 000 cm^{-1} wave numbers (8066 cm^{-1} = 1 eV) on a 100 x 100 μm^2 single crystal up to 3.5 GPa using a BETSA membrane diamond anvil cell. A closed cycle cryostat was used to cool down the sample. The sample was loaded inside a stainless-steel gasket hole together with KBr as a hydrostatic medium. The gasket was used as a reference mirror. R_{sd} (ω) was measured by using a homemade high-vacuum microscope including an X15 Schwarzchild objective connected to a BRUKER IFS 66v/S Fourier Transform Spectrometer with a Mercury-Cadmium-Telluride detector and thermal light sources. Pressure was measured with the standard ruby fluorescence technique. Measurements were performed at fixed temperature (40 K) by increasing the pressure. To obtain the optical conductivity from the R_{sd} (ω), we used the variational dielectric function method [56].

Data availability

Data sets generated during the current study are available from the corresponding authors on reasonable request.

References

[51] Querré, M. *et al.* Non-volatile resistive switching in the Mott insulator $(V_{1-x}Cr_x)_2O_3$. *Physica B: Condensed Matter* **536**, 327–330 (2018). doi: 10.1016/j.physb.2017.10.060

[52] Thomas, G. A. *et al.* Observation of the Gap and Kinetic Energy in a Correlated Insulator. *Phys. Rev. Lett.* **73**, 1529–1532 (1994). doi: 10.1103/PhysRevLett.73.1529

[53] Baldassarre, L. *et al.* Quasiparticle evolution and pseudogap formation in V_2O_3: An infrared spectroscopy study. *Phys. Rev. B* **77**, 113107 (2008). doi: 10.1103/PhysRevB.77.113107

[54] Stewart, M. K. *et al.* Insulator-to-metal transition and correlated metallic state of V_2O_3 investigated by optical spectroscopy. *Phys. Rev. B* **85**, 205113 (2012). doi: 10.1103/PhysRevB.85.205113

[55] Cammarata, M. *et al.* Chopper system for time resolved experiments with synchrotron radiation. *Review of Scientific Instruments* **80**, 015101 (2009). doi: 10.1063/1.3036983

[56] Kuzmenko A. B., Kramers-Kronig constrained variational analysis of optical spectra, Rev. Sci. Instrum. 76, 083108 (2005). doi: 10.1063/1.1979470

[57] Coelho, A. A. TOPAS and TOPAS-Academic: an optimization program integrating computer algebra and crystallographic objects written in C++. *J Appl Cryst* **51**, 210–218 (2018). doi:10.1107/S1600576718000183

[58] Thompson, P., Cox, D. E. & Hastings, J. B. Rietveld refinement of Debye–Scherrer synchrotron X-ray data from Al2O3. *J Appl Cryst* **20**, 79–83 (1987). doi: 10.1107/S0021889887087090

[59] Mandal R. Time-resolved XRD study of size dependence in the photoinduced phase change in transition metal oxides. PhD thesis, University of Rennes (2023). https://univ-rennes.hal.science/UR1-THESES/tel-04544262v1

Acknowledgements

M.Lo. and E.J gratefully acknowledge the Agence Nationale de la Recherche for financial support under grants ANR-16-CE30-0018 (“Elastica”), ANR-19-CE29-0018 (“Multicross“) and ANR-23-CE30-0027 (“FASTRAIN”). S.I. acknowledges JST CREST (JPMJCR1901), MEXT Q-LEAP (JPMXS0118067426) for their financial supports. L.C. acknowledges the Région Pays de la Loire for its financial support through the Mott-IA project. EP thanks the support of the CNRS and the French Agence Nationale de la Recherche (ANR), under grant ANR-22-CPJ2-0053-01. Funded/Co-funded by the European Union (ERC, PhotoDefect, 101076203).Views and opinions expressed are however those of the author(s) only and do not necessarily reflect those of the European Union or the European Research Council. Neither the European Union nor the granting authority can be held responsible for them.

We thank MAX IV synchrotron source for the access to time-resolved x-ray diffraction experiment at the FemtoMAX beamline in Lund, Sweden. We acknowledge the European Synchrotron Radiation Facility (ESRF) for provision of synchrotron radiation facilities and use of beamline ID09, and thank R. Garlet, B. Richer and Y. Watier for their help in setting up the cryo cooling system.

We thank A. Merabet for preparing the FIB lamella extracted from one of the thin films studied in this paper. Some measurements were performed using the IMN’s characterisation platform, PLASSMAT, Nantes, France. We thank the financial support by the NExt initiative through national funding by the French National Research Agency (ANR) under the Programme d'investissements d'Avenir (reference ANR-16-IDEX-0007). "

Authors contributions

H.C., M.Lo., S.I., E.J. coordinated the project. T.A., H. I., Y. K. and S. I. performed and analysed the time-resolved reflectivity experiments. Y.N., H.K. measured the steady state reflectivity on thin films. V.TP. and R.S. built the setup for high pressure reflectivity, and with help of B.C. and D.B. measured the single crystal. A.J., V.-T.P, D.K., J.C.E., B.A. and J.L. developed the FemtoMAX setup for time-resolved X-Ray diffraction. R.M., J.G.-B., A.V., E.T., M.S., E.P., M. A., E.J. and M. Lo. proposed the experiment at FemtoMAX and performed it with the help of local contacts. C.M., M.Le. and M.K. designed the ESRF tr-XRD experiment. J.G.-B., R.M., E.T., M.S., B.C., and E.J. performed the experiment at ESRF. R.M., J.G.-B., A.V. analysed tr-XRD data. J.G.-B. established the correction function for sample displacement adapted to the geometry of the FEMTOMAX beamline. D.B., J.T., B.C., E.J. and L.C. prepared and

characterized the thin films and single crystals. M. D. performed the STEM study. H.C., M.Lo., S.I., E.J., B.C. and L.C. analysed and discussed closely about the whole results. H.C., M.Lo., S.I., E.J., wrote the manuscript with significant contributions from C.M. and E.P., critical reading from J.L., A.J., V.-T.P., and help from all coauthors.

Competing interest

The authors declare no competing interests.

Extended Data

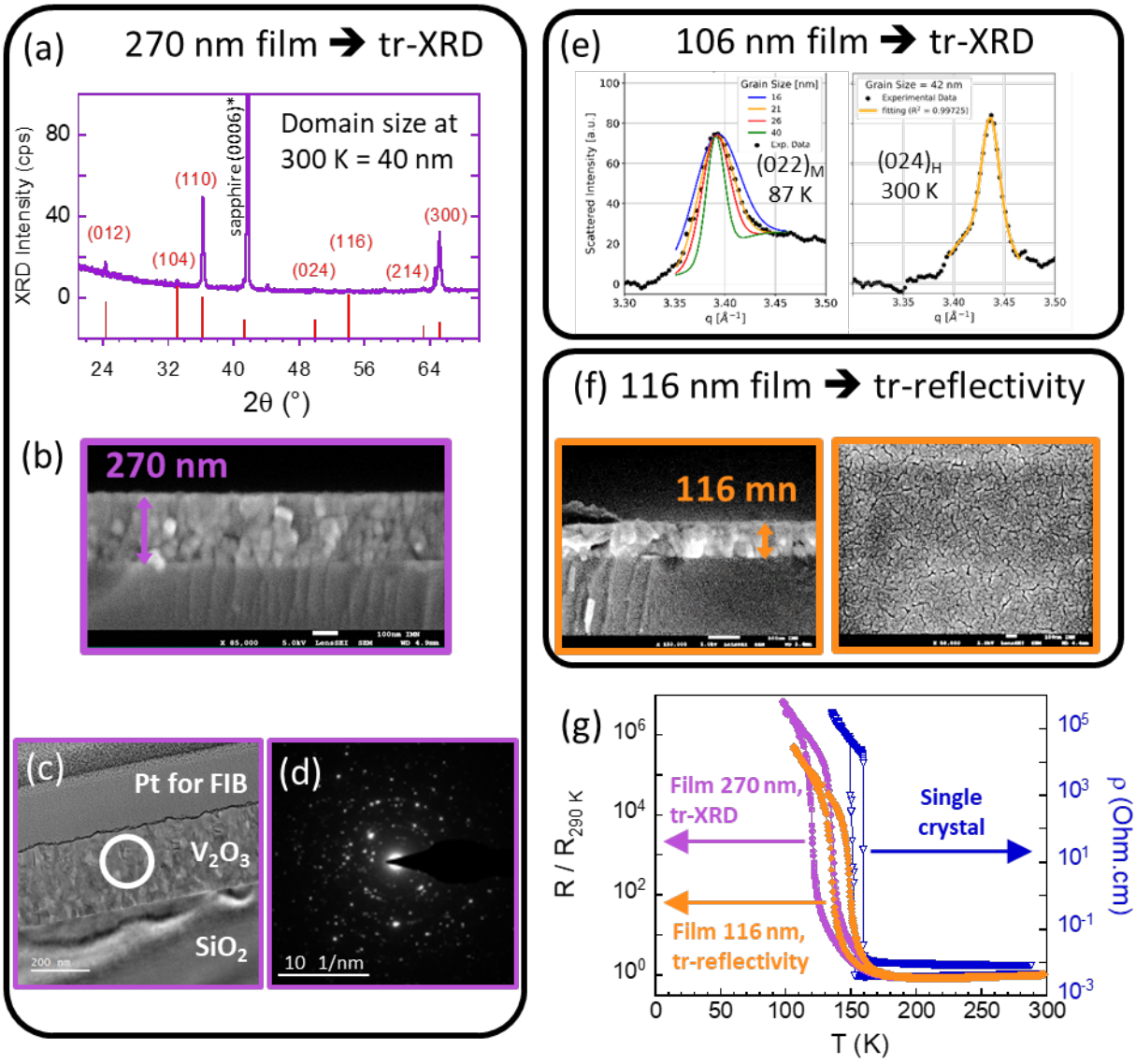

Extended data Fig.1 | Characterization of the V_2O_3 single crystal and thin films used in the work.

(a) Steady-state X-Ray diffraction (XRD) pattern measured in a Bragg-Brentano geometry on the 270 nm thick film used for time-resolved XRD. The average crystallite size at room temperature, estimated by the Scherrer formula, is 40 ± 5 nm. Compared to theoretical intensities (red bars), the enhancement of (*hk0*) Bragg peaks with respect to other (*hkl*) indicates a preferential orientation with the *c*-axis of the grains mostly oriented parallel to the substrate surface (see Extended Data Fig.8).
(b): Scanning Electron Microscopy (SEM) image of a similar film prepared together with the previous one, but deposited on a SiO_2/Si substrate, and allowing a reliable estimate of the thickness.
(c) TEM image of the film shown in (b) measured on the S/TEM Themis Z G3 electron microscope, (Thermo Fisher Scientific). This TEM sample was prepared by Focus Ion

Beam (FIB) in a ZEISS Crossbeam 550L scanning electron microscope. The white circle indicates the typical beam size used for collect electron diffraction images shown in (d).
(d) Representative electron diffraction image collected close to the free surface. In (c), the free surface was covered by Platinum during FIB lamella preparation process. The electron diffraction images show exclusively Bragg peaks diffracted by multiple grains hit by the electron beam and absolutely no trace of amorphous phase. This rules out the possibility that the 9 ps delay for volume change shown in Fig.4 b is related to an thick amorphous phase at the surface of the V_2O_3 films.
(e) XRD pattern of the 106 nm thick film used for tr-XRD both at ID09 and FemtoMAX beamlines. Zoom on the $(024)_H$ Bragg peak in PM phase, $(022)_M$ peak below the PM to AFI transition temperature, measured under steady state at ID09. A clear broadening of this Bragg peak appears in the monoclinic phase. Simulation of the $(022)_M$ Bragg peak leads to an estimate of the ferroelastic monoclinic domains size of 20±5 nm (➔ average radius = 10 ± 2.5 nm). This diffracting domain is half that at 300 K (see simulation of Bragg peak with a domain size of 40 nm).
(f) SEM images (side and top views) of a 116 nm film prepared together with the one used for tr-reflectivity, but deposited on a SiO_2/Si substrate.
(g) Temperature dependence of resistivity (single crystal) and resistance (thin films) of the samples used in this study. The large amplitude of the resistivity jump at the transition and the high transition temperature (160K upon heating) attest the quality and stoichiometry of the single crystal. Crystals from the same batch are used both for steady state and time-resolved reflectivity. The films show a jump of similar amplitude at the transition, with a slightly reduced transition temperature (147 K upon heating on the 116 nm thick film) as usually observed in V_2O_3 films. The absence of hysteresis below 120 K (tr-reflectivity thin film) and 107 K (tr-XRD) ensures the absence of phase coexistence in the different time-resolved studies performed in this work.

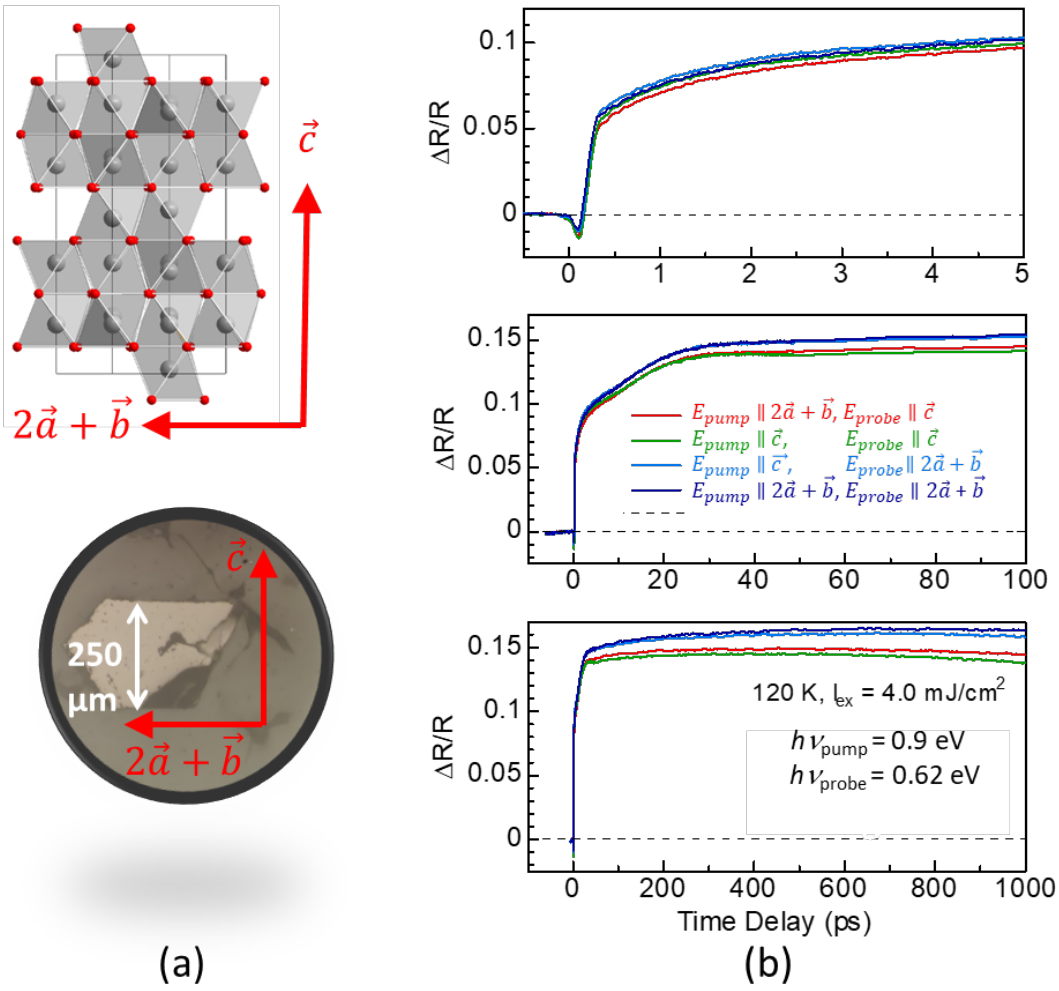

Extended data Fig.2 | Effect of single crystal orientation and pump/probe laser polarization on time-resolved reflectivity in the AFI state of V_2O_3. In Fig.2 of the main article, we unveil a weaker photoinduced response of the single crystal with respect to thin film. In order to check if it results from an anisotropic response of V_2O_3, we have performed polarization dependent tr-reflectivity after a proper orientation of a V_2O_3 single crystal by XRD and a polishing to reveal a surface suitable for tr-reflectivitty. (a) optical image of the V_2O_3 crystal used for tr-reflectivity, with a surface defined by the the directions $\vec{c}$ and $2\vec{a}+\vec{b}$. (b) time-resolved reflectivity performed with polarization directions of the pump and the probe aligned along the $\vec{c}$ and $2\vec{a}+\vec{b}$ directions after photoexcitation at 4 mJ.cm^{-2} at 120 K. Overall, the polarization effect is very weak and is hence not the cause of the weaker photoinduced response of the crystal shown in Fig.2 of the main text.

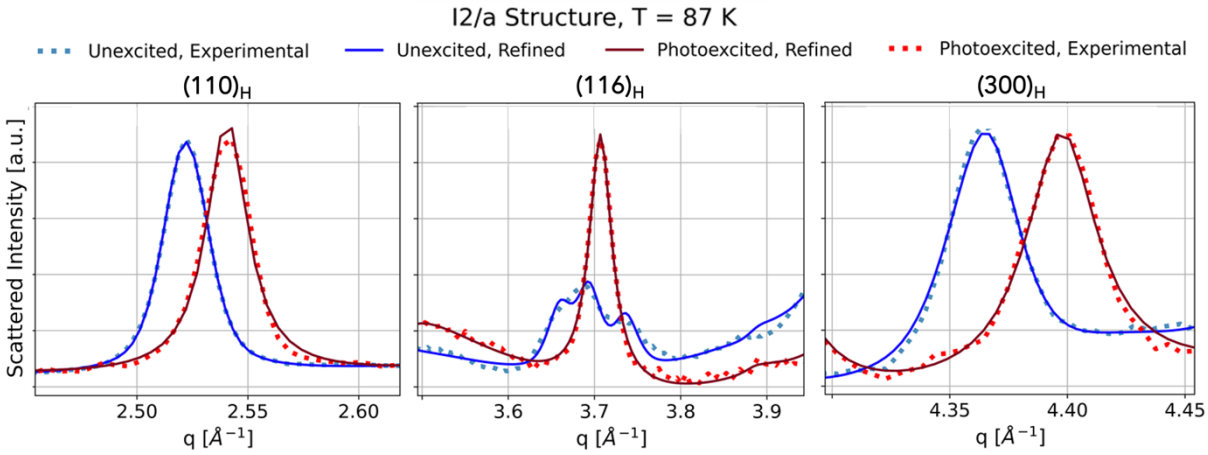

Extended data Fig.3 | X-Ray diffraction patterns measured at ID09 on V_2O_3 thin film (106 nm) at 87 K in the AFI monoclinic phase. The dashed lines correspond to XRD patterns without (blue) and with (red) photoexcitation of 10.5 mJ/cm² (delay 400 ps) converting 100 % of the volume into a metallic hexagonal phase. These XRD patterns were refined with Rietveld method (blue and red lines), allowing to extract the monoclinic cell parameters (space group 15, I2/a). We found for the unexcited initial phase:

a_M = 7.321(3) Å, b_M = 4.988(1) Å, c_M = 5.5325(28) Å, β = 96.96(2)°, V_M = 200.54(15) Å^3

and

a_M = 7.364(7) Å, b_M = 4.953(2) Å, c_M = 5.464(7) Å, β = 97.63(4)°, V_M = 197.54(15) Å^3 for the photo-excited phase 100 % converted into the hexagonal phase (delay = 400ps, fluence = 10.5 mJ/cm²).

As the photo-conversion towards the hexagonal phase is complete, the photo-induced XRD pattern can equally be refined with a hexagonal unit cell, yielding a_H = 4.9505(6) Å, c_H = 13.966(6) Å and hence 2/3*V_H = 197.6 (2) Å^3.

Overall, the photoinduced volume change $\Delta V/V$ determined with this refinement procedure amounts to -1.50 $\pm$ 0.12 %.

However this refinement procedure is tedious and requires advanced corrections of sample to detector distance drifts. Therefore we used another strategy to estimate the volume change at any time delay and fluence, based on the simple Q shift of the $(110)_H$ Bragg peak. This is justified since:

(1) the photoinduced change of the pseudo-hexagonal c_H parameter (determined as $c_H = 2\sqrt{c_M^2 + \frac{1}{4}a_M^2 - a_M c_M \cos\beta}$) is as low as $\Delta c_H/c_H$ = +0.16 %, demonstrating that most of the volume change result from the large decrease of the pseudo-hexagonal a_H parameter,

(2) the refinement demonstrates that the two monoclinic Bragg peaks deriving from the $(110)_H$, *i.e.* the $(020)_M$ and $(211)_M$, are almost superimposed in the monoclinic phase ($Q_{(211)_M} - Q_{(020)_M} < 0.004$ Å^{-1}).

As a consequence, the photoinduced shift ΔQ of the $(110)_H$ Bragg peak directly gives the relative change of the pseudo-hexagonal a_H parameter $\Delta Q/Q = -\Delta a_H/a_H$ and the relative volume change $\Delta V_H/V_H = 2\ \Delta a_H/a_H + \Delta c_H/c_H \approx 2\ \Delta a_H/a_H$. In the example shown in Extended Data Fig. 3, this method yields $\Delta V_H/V_H$ = -1.48 $\pm$ 0.10 %, in perfect agreement with the refinement method. All the estimate of the volume changes presented in Fig.3 and Fig.4 are obtained using this strategy.

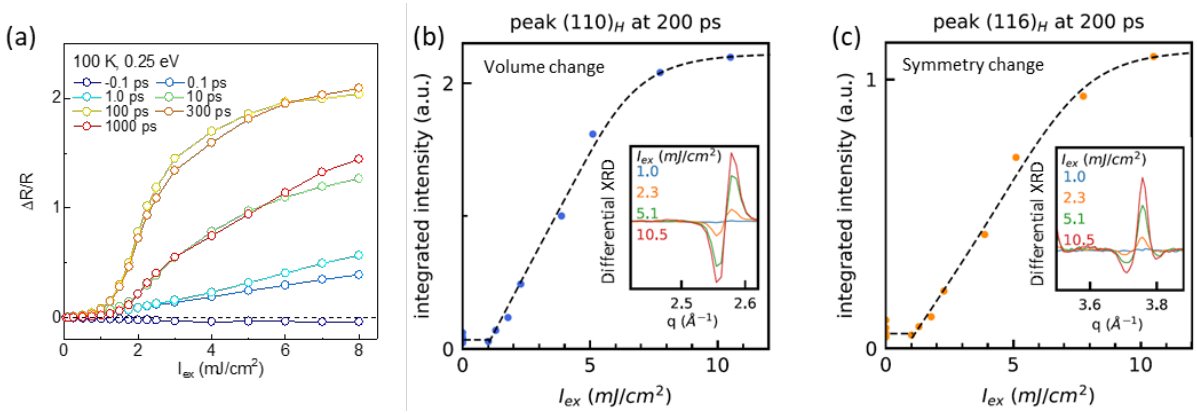

Extended data Fig.4 | Evolution of transient reflectivity and time-resolved XRD with fluence in the 85-100 K temperature range. (a) Evolution of transient reflectivity with fluence measured on the same 116 nm film as in Fig.3a, the same conditions (pump 0.89 eV, probe at 0.25 eV), but at 100 K instead of 10 K. (b) Fluence dependency of the volume change measured at 87 K on the 106 nm film (see Methods), as deduced from the integration of the differential XRD pattern around the $(110)_H$ Bragg peak for a pump-probe delay of 200 ps (c) Same as (b) for the symmetry change, deduced from the integration of differential XRD around the $(116)_H$ peak.

These three plots unveil a clear threshold fluence around 1 mJ/cm² above which the electronic part (a) and the structural components (b and c) of the insulator-to-metal transition are initiated. The threshold is reduced from 2.5 mJ/cm² at 10K (see Fig.3) to 1 mJ/cm² around 85-100 K

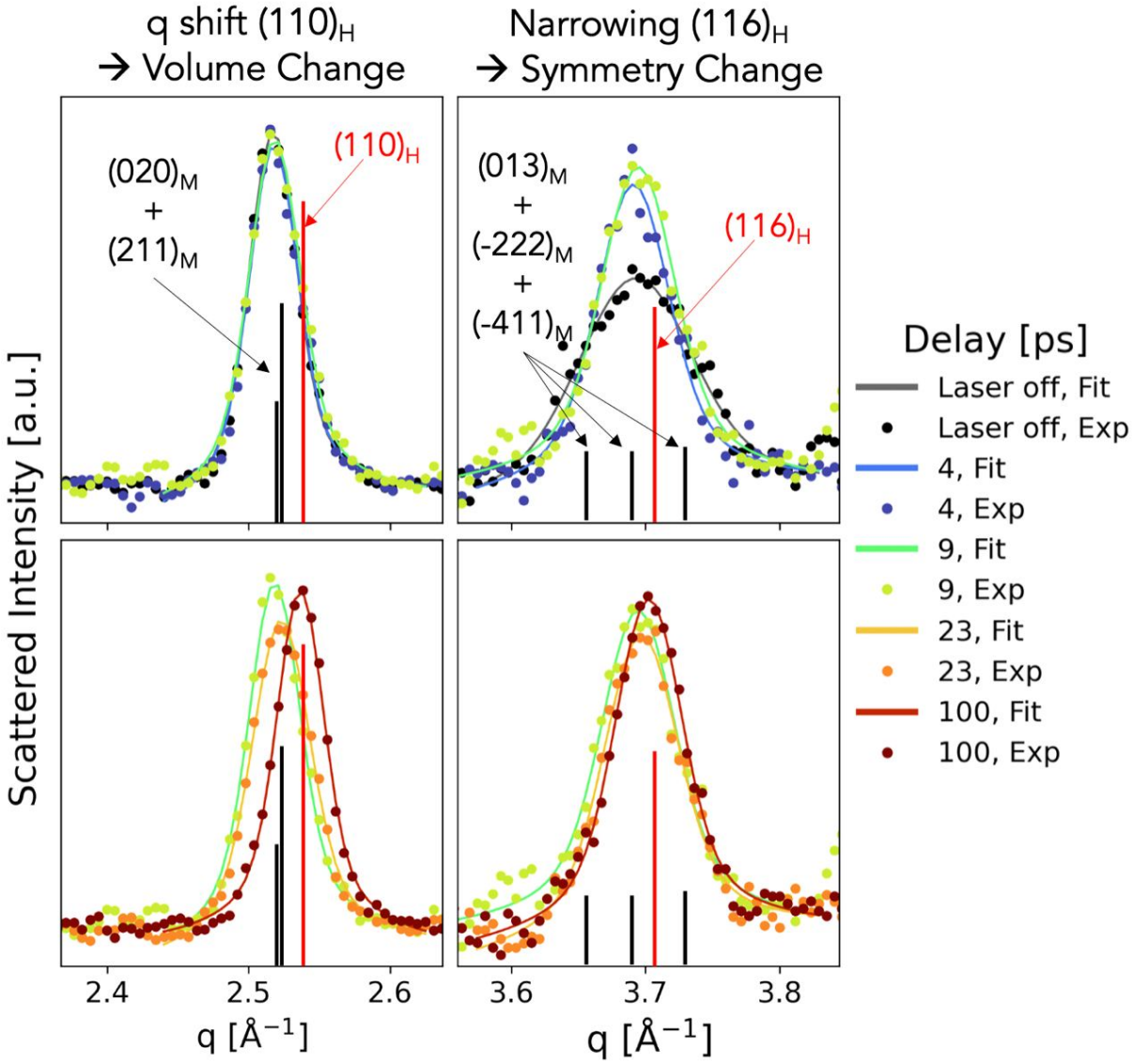

Extended data Fig.5 | Evidence of different time scale for symmetry and volume change from time-resolvd XRD, measured at 10K on the 270 nm film at FemtoMAX. (Left) Evolution of the $(110)_H$ Bragg peak for pump-probe delays shorter (top) and longer (bottom) than 9 ps. (Right) Same for the $(116)_H$ Bragg peak, split into three peaks $(013)_M$, $(-222)_M$ and $(-411)_M$ in the initial monoclinic state.

Vertical bars indicate the Bragg peak positions from the refinement of XRD pattern of the 116 nm film shown in Extended Data Fig.3, in black monoclinic, in red hexagonal phase. These panels evidence that the monoclinic to hexagonal transition is completed in less than 4 ps (see top right part), whereas volume change occurs slower after a onset shift of roughly 9 ps (left part). The fitting procedure of the individual peaks is described in the Methods section.The key results shown in Fig.4, *i.e.* the temporal evolution of the symmetry and volume changes, are extracted from the fitted FWHM of the $(116)_H$ and shift of the $(110)_H$ peaks, respectively (see complementary discussion in Extended Data Fig.3).

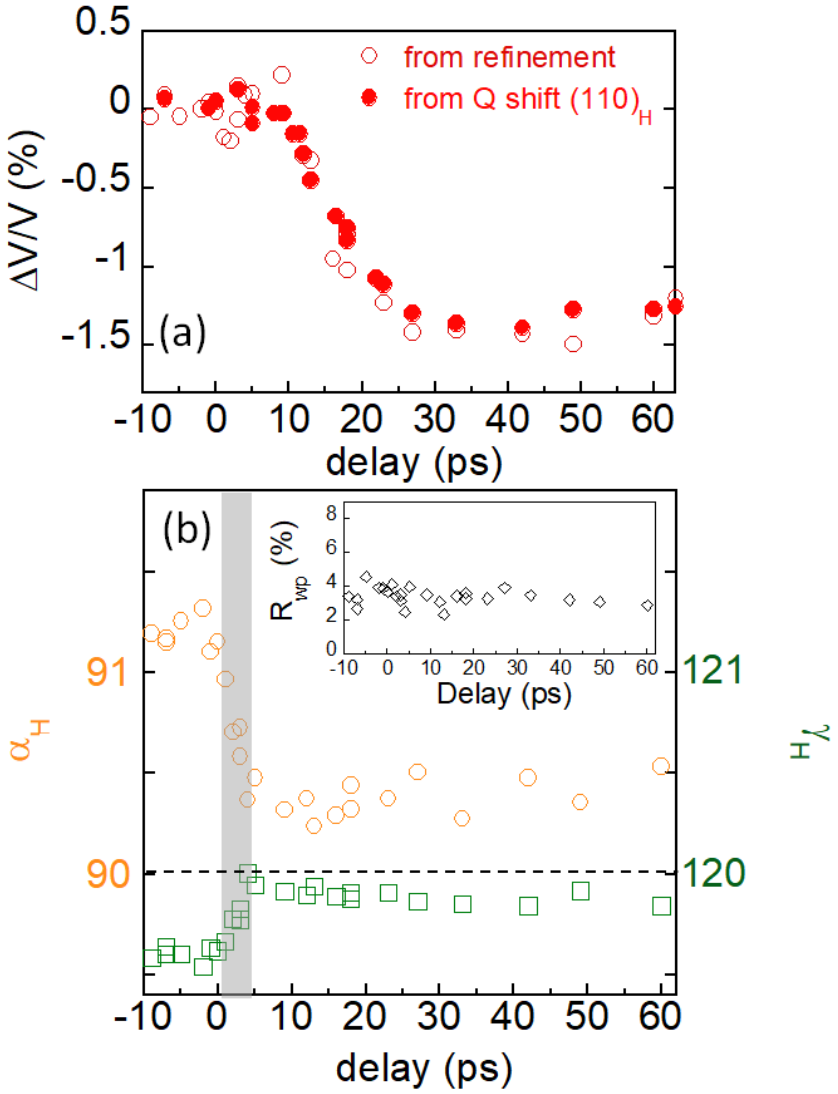

Extended Fig. 6 | Results of XRD powder pattern refinements measured at Femtomax on the thin (106 nm) V_2O_3 film. (a) Temporal evolution of the unit cell volume change evaluated by the Q-shift of the $(110)_H$ Bragg peak, as used in Fig.4 of the article, and by the whole powder pattern refinement. Both methods lead to the same conclusion, *i.e*. that the average volume is unchanged during the first 9 ps, before decreasing during 16 ps (time required for a strain wave propagating at the speed of sound to travel though the film from the surface to the substrate). (b) Time dependence of the α_H and γ_H angles of the pseudo-hexagonal unit cell (see description below). The evolution of α_H and γ_H is similar with the time dependence of $(116)_H$'s FWHM displayed in Fig.4a, with a very fast evolution during the first ps and a plateau reached after less than 4 ps. Moreover, the values of α_H and γ_H at the plateau are extremely close to those expected for a $R\bar{3}c$ symmetry, *i.e.* 90° and 120° respectively. Inset: temporal evolution of R_{wp} showing that the quality of the refinement is essentially time-independent.

The whole pattern refinement was performed using the Topas software [57]. Peak shape was described using TCHZ function [58]. Spherical harmonics intensity correction was used to account for the preferred orientation. Sample displacement was refined for interleave reference patterns with no laser. It was then used as starting point

for the refinement of the following “laser on” pattern, in order to correct from any residual sample-to-detector drift. Additional information about data reduction and refinement methods can be found in Ref. [59]. A correction function for sample displacement well adapted to the geometry of the Femtomax beamline (see Methods) was used:

$$2\theta_c = 2\theta_u + \arctan\left(\frac{\Delta.\sin(4\theta_u)\,[1+\tan(2\theta_u)\tan\phi]}{2[D_u - \Delta\cos^2(2\theta_u).(1+\tan(2\theta_u)\tan\phi)]}\right)$$

where $\phi \approx 30°$ corresponds to the tilt of the detector, θ_c and θ_u are the corrected and uncorrected values of the diffraction angles, D_u is the uncorrected sample to detector distance, Δ is correction for the sample to detector distance (corrected sample to detector $D_{corrected} = D_u - \Delta$).

The refinements were performed in the monoclinic *I*2/*a* space group [26]. The obtained monoclinic cell was then transformed into the non-primitive pseudo-hexagonal cell thanks to the matrix

$$\begin{pmatrix}\overrightarrow{a_H}\\ \overrightarrow{b_H}\\ \overrightarrow{c_H}\end{pmatrix} = \begin{pmatrix}0 & 1 & 0\\ 1/2 & -1/2 & 1/2\\ 1 & 0 & -2\end{pmatrix}\begin{pmatrix}\overrightarrow{a_M}\\ \overrightarrow{b_M}\\ \overrightarrow{c_M}\end{pmatrix}$$

as recently proposed in Ref. [17]. With such a choice, the refined pseudo-hexagonal angles in the film at steady state are $\alpha_H \approx 91.2°$, $\beta_H = 90°$ and $\gamma_H \approx 119.6°$ (see Extended Data Fig. 6b), as opposed to the hexagonal parameters $\alpha_H = \beta_H = 90°$ and $\gamma_H = 120°$.

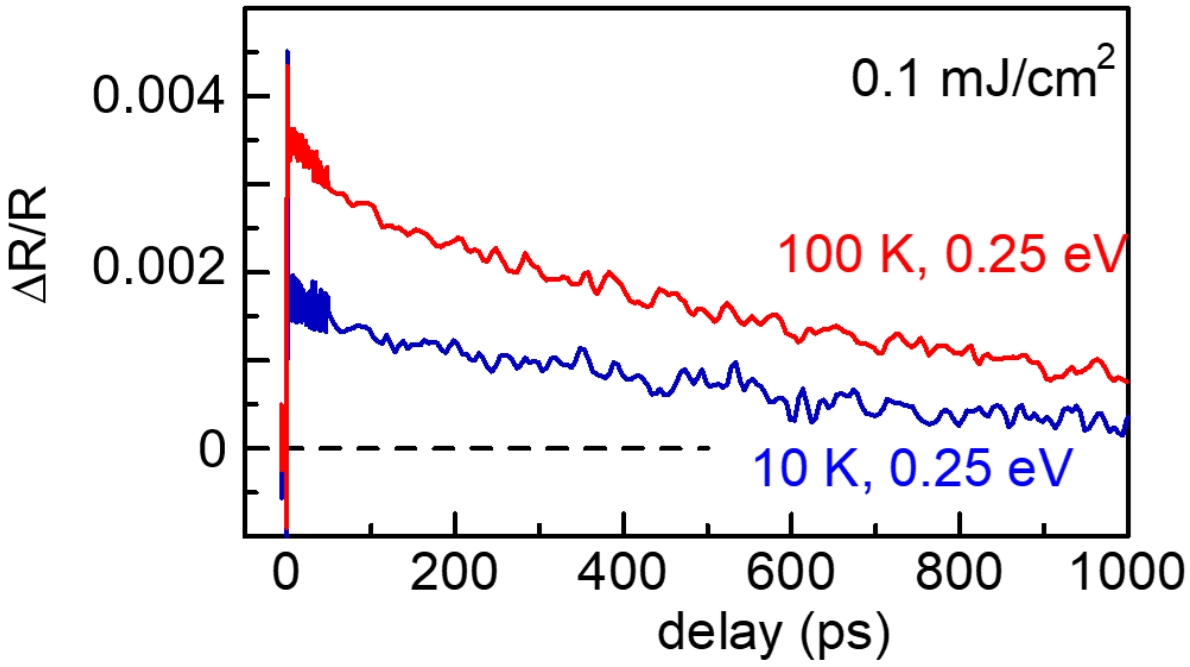

Extended data Fig.7 | **Evidence of long-lived hot electronic states from transient reflectivity data.** Time-resolved reflectivity measured at low pump laser fluence (0.1 mJ/cm², photon energy = 0.89 eV), showing electronic recombination time in the nanosecond range.

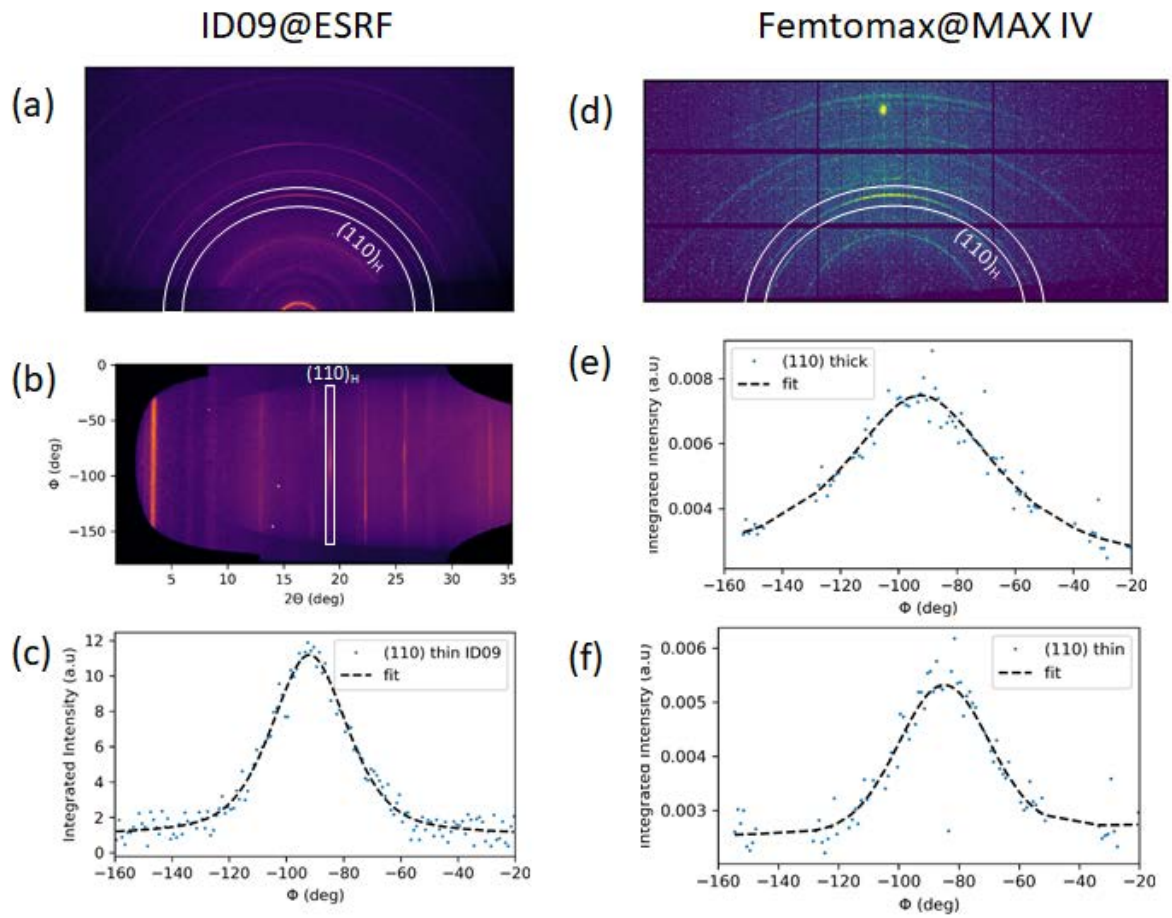

Extended Data Fig.8 | Typical 2D detector images measured a) at ID09 on the 2D Rayonix CCD detector and d) at Femtomax on the 2D pilatus photon counting detector. b) The unfolded ID09 image shows the available azimuthal range. c), e) and f) Intensity along the $(110)_H$ Bragg peak for the thin film measured at ID09 (106 nm), and for the thick (270 nm) and thin (106 nm) film measured at Femtomax, respectively. The intensity is integrated over 1 deg and 1.5 deg for Femtomax and ID09 data respectively. These profiles were refined using a pseudo Voigt function with linear background:

$$I = (1-\Gamma).A.exp\left(\frac{(x-x_0)^2}{2\sigma^2}\right) + \Gamma.A.\frac{\sigma^2}{(x-x_0)^2+\sigma^2} + y_0 + y_1.x$$

σ was found equal to 16 degrees and 18 degrees for the thin films (for ID09 c) and Femtomax f) profiles respectively) and to 30 degrees for the thick film (Femtomax profile e))

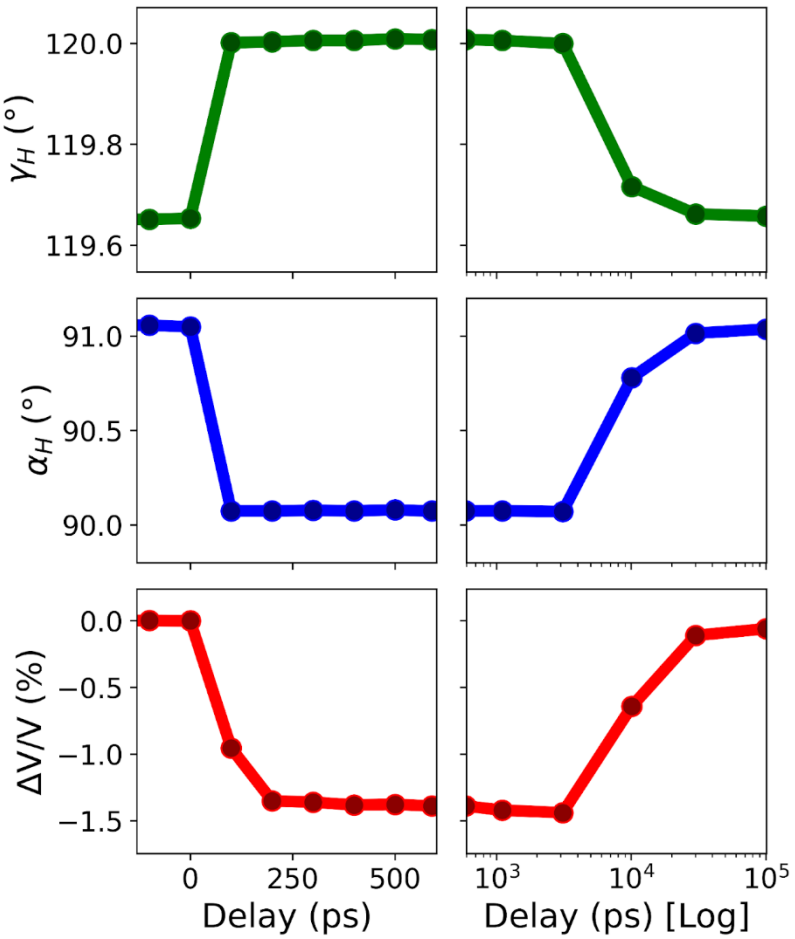

Extended Data Fig.9 | Structural evidence for a long plateau of time-independent structural change between 100 ps and 3 ns after initial photoexcitation, followed by a complete relaxation in the 3-100 ns range in the thin film (106 nm) measured at ID09 at 87 K and for a fluence (10.5 mJ/cm²) inducing a full AFI-to-PM transformation. (a) and (b) Temporal evolution of γ_H and α_H, angles of the pseudo-hexagonal unit cell (see definition in Extended Data Fig. 6) evidencing the photoinduced symmetry change to the hexagonal symmetry ($\gamma_H \approx 120°$ and $\alpha_H \approx 90°$) lasting up to 3 ns, and its relaxation towards the monoclinic symmetry ($\gamma_H \approx 119.65° \neq 120°$ and $\alpha_H \approx 91.1° \neq 90°$). (c) Temporal evolution of the relative volume change, showing a plateau at -1.5 % up to 3 ns, and then relaxing to its initial value between 3 and 100 ns.